Behavior of the Discontinuous Galerkin Method for Compressible Flows at Low Mach Number on Triangles and Tetrahedrons

Jonathan Jung, Vincent Perrier

BEHAVIOR OF THE DISCONTINUOUS GALERKIN METHOD FOR COMPRESSIBLE FLOWS AT LOW MACH NUMBER ON TRIANGLES AND TETRAHEDRONS

JONATHAN JUNG* AND VINCENT PERRIER†

Abstract. In this article, we are interested in the behavior of discontinuous Galerkin schemes for compressible flows in the low Mach number limit. We prove that for any numerical flux conserving exactly contacts (e.g., exact Godunov, Roe, HLLC), the numerical scheme is accurate at low Mach number flows on simplicial meshes, which is an extension to higher order of the result proven in [20]. When the mesh is not simplicial, or when the mesh is simplicial but the numerical flux does not conserve contacts (e.g., Lax–Friedrich, HLL), the scheme is numerically proven to be less accurate in the low Mach number limit.

Key words. discontinuous Galerkin methods, wave system, Euler system, long time limit, low Mach number limit

MSC codes. 65M60,65M08,65M12,65M22,76N99.

1. Introduction. The aim of this article is to study the accuracy of the discontinuous Galerkin method at a low Mach number. The discontinuous Galerkin method is a finite element method with piecewise discontinuous polynomials, and can be seen as a high order extension of finite volume schemes, and matches exactly with it when all the polynomials have a degree zero.

When the Mach number goes to zero, two main difficulties occur with finite volume schemes: time integration and low Mach number accuracy. Time integration difficulty is due to the great disparity at low Mach number between the speed of material waves (slow) and acoustic waves (fast). Classical explicit solvers are constrained by a CFL restriction on the time step induced by the acoustic waves. Then, at low Mach number, the time step becomes of the order of the Mach number and explicit solvers are no longer efficient for the computation of convective phenomena. Fully implicit time stepping can be considered, but it leads to solving a nonlinear system at each time step, which is very costly. An intermediate solution was developed over the last three decades, which aims at getting an Implicit-Explicit (ImEx) method which needs a single linear system to solve at each time step; see [12] for the isentropic Euler system and [11] for the full Euler system. In [15], this ImEx method was coupled with an adaptive tuning of the viscosity for addressing both the low Mach number accuracy and the time integration problem. This method was extended to second order in [14] for the isentropic Euler system and in [5] for the full Euler system. Note that some variations exist in the splitting of the Euler flux into a linear term (representing acoustics and discretized implicitly) and the nonlinear remainder: [30, 37] proposed to use Klein's nonstiff/stiff decomposition of the fluxes [28], whereas in [23, 7] a dynamical Mach number dependent (dependent in time) splitting was proposed. These ImEx methods have not been limited to Euler systems: two-phase flows systems were addressed, for example, in [10], whereas in [37], the Euler system with gravity source terms was addressed. The stability of such a method was, for example, addressed in [31], where the stability in the sense of mathematical entropy is proven under an advective CFL number linked with the slow waves. This allows to use larger time steps at low Mach number.

The second difficulty concerns the low Mach number limit of the compressible discrete solution and is referred to in the rest of the paper as the *low Mach number accuracy problem*. At the continuous level, for well-prepared data, the solution of the compressible Euler equations converges toward the solution of the incompressible Euler equations as the Mach number tends to zero [26]. However, at the discrete level this property is in general not satisfied for classical finite volume schemes. Issues were first reported in [39]. The problem is induced by the spatial discretization and is independent of the time integration. This strongly depends on the choice of the numerical flux. An extensive literature exists on the topic; see [21] and references therein for a very complete review. Several solutions were reported for curing the low accuracy when the Mach number goes to zero [22, 33]. These fixes consist in modifying the numerical diffusion of the scheme in the low Mach number regime. From this point of view, the semi-implicit solvers previously mentioned also use low Mach number fixes because in general a centered discretization of the pressure gradient is used for the spatial discretization of the pressure gradient (which is then integrated implicitly in time in the case of the semi-implicit method). Other

*LMA, UPPA, Pau, France and Cagire team, Inria Bordeaux Sud-Ouest, France jonathan.jung@univ-pau.fr.
†Cagire team, Inria Bordeaux Sud-Ouest, France and LMA, UPPA, Pau, France, vincent.perrier@inria.fr.

types of spatial discretizations, accurate at low Mach number, have recently been proposed, more precisely using a nodal solver for the computation of the numerical fluxes [2, 18] or using staggered schemes [1, 36, 6, 9].

This paper is focused on the low Mach number accuracy of classical discontinuous Galerkin schemes, more precisely on the impact of the cell geometry on the accuracy. In [34, 20], a quite surprising result was reported: the cell geometry has an influence on the low Mach number accuracy of the Roe finite volume scheme. More precisely, when the Mach number goes to zero, the Roe scheme is accurate on triangles and tetrahedrons, but not accurate on the other types of cells. The HLL scheme is not accurate at low Mach number, neither on quadrangular mesh nor on triangular mesh [32]. In [24, 25], it was remarked that the numerical fluxes could be separated into two families: the ones that are asymptotically consistent [1] with a Godunov flux for a linear wave system, which are accurate at low Mach number on triangles and tetrahedrons, and the ones that are asymptotically consistent with a Rusanov flux for a linear wave system, which are not accurate at low Mach number.

As far as collocated discontinuous Galerkin methods are concerned, very few studies have been performed. If a focus is made on density based solvers, not on pressure based solvers such as developed in [41], the literature is basically restricted to [3] and [16]. In [3], implicit computations of stationary low Mach number flows are performed. It was reported that using low Mach number fixes of type [22] improves the accuracy on quadrangular meshes and improves the conditioning of the matrix for implicit computations, therefore improving the convergence velocity toward the stationary solution. On triangles, the results with and without fixes show similar accuracy. In [16], the numerical method is based on the Vijayasundaram flux on triangular meshes (which, as remarked in [40], is similar to the Roe flux, where the Roe average is replaced by a simple arithmetic average). No special fix is used when the Mach number goes to zero. The results of these two articles suggest that the influence of the cell geometry reported in [34, 20] for finite volume schemes holds also for the discontinuous Galerkin method.

In this article, we propose to prove and numerically illustrate that on simplicial meshes, the discontinuous Galerkin method based on numerical fluxes that preserve contacts always have a good accuracy when the Mach number goes to zero. We also make numerical evidence that this is not the case for numerical schemes that do not preserve contacts, and that numerical schemes on quads have a low accuracy in general. This paper is organized as follows. In section 3, the discontinuous Galerkin method is recalled, and the numerical scheme is expanded in power of the Mach number. This leads to two types of asymptotic schemes: the ones that preserve the contacts, and the ones that do not. In the case of preservation of contacts, we prove in section 4 that on triangles and tetrahedrons, the first order pressure is uniformly equal to zero, and that the zeroth order velocity follows a discrete zero divergence equation, leading to a good accuracy at low Mach number. In section 5, all these statements are numerically tested. Last, section 6 is a conclusion.

2. Link between the low Mach number problem and the long time limit of the wave system.

2.1. The model and its formal asymptotic behavior when the Mach number goes to zero. We consider the isentropic Euler model

$$\left\{ \begin{array}{l} \partial_t \rho + \nabla \cdot (\rho \mathbf{u}) = 0, \\ \partial_t (\rho \mathbf{u}) + \nabla \cdot (\rho \mathbf{u} \otimes \mathbf{u}) + \nabla p = 0, \end{array} \right. \tag{2.1}$$

where ρ is the density, p the pressure, and $\mathbf{u}$ the velocity. The system is closed by an equation of state $p = p(\rho)$, which is supposed to be a convex function. We denote then by a the sound velocity, $a = \sqrt{p'(\rho)}$. We are interested in a Cauchy problem for (2.1), namely the density ρ and the velocity $\mathbf{u}$ are supposed to be known at $t = 0$. This paper deals with flow on a bounded domain. This means that a density ρ_b and a velocity $\mathbf{u}_b$ are weakly imposed on the boundary of the domain Ω. In particular, we will consider two types of boundary conditions:

- wall boundary condition with $(\rho_i, \mathbf{u}_i)$ as internal state,

$$\left[\begin{array}{c} (\rho \mathbf{u}) \cdot \mathbf{n} \\ (\rho \mathbf{u}) (\mathbf{u} \cdot \mathbf{n}) + p(\rho) \mathbf{n} \end{array} \right]_{\text{Wall}} = \left(\begin{array}{c} 0 \\ p(\rho_i) \mathbf{n} + a(\rho_i) (\rho_i \mathbf{u}_i \cdot \mathbf{n}) \mathbf{n} \end{array} \right); \tag{2.2a}$$

[1] The exact meaning of this asymptotic consistency is detailed in [25] and will be recalled in section 2 of this article.

- inlet/outlet boundary condition, between an internal state $(\rho_i, \mathbf{u}_i)$ and a weakly imposed state $(\rho_b, \mathbf{u}_b)$, which relies on the Steger–Warming weakly imposed state (see [25, Appendix A] for details),

$$\begin{aligned}\begin{bmatrix} (\rho\mathbf{u})\cdot\mathbf{n} \\ (\rho\mathbf{u})\,(\mathbf{u}\cdot\mathbf{n}) + p(\rho)\mathbf{n} \end{bmatrix}_{\mathrm{SW}} &= \frac{1}{2}(\mathbf{u}_b\cdot\mathbf{n} + a_b)\left[\rho_i + \frac{\rho_i}{a_b}(\mathbf{u}_i - \mathbf{u}_b)\cdot\mathbf{n}\right]\begin{pmatrix} 1 \\ \mathbf{u}_b + a_b\mathbf{n} \end{pmatrix} \\ &\quad + (\mathbf{u}_b\cdot\mathbf{n})^+\rho_i\begin{pmatrix} 0 \\ (\mathbf{u}_i - \mathbf{u}_b)^\perp(\mathbf{n}) \end{pmatrix} \\ &\quad + \frac{1}{2}(\mathbf{u}_b\cdot\mathbf{n} - a_b)\rho_b\begin{pmatrix} 1 \\ \mathbf{u}_b - a_b\mathbf{n} \end{pmatrix}.\end{aligned} \tag{2.2b}$$

For studying the behavior of system (2.1) in the low Mach number regime, three characteristic scales are supposed to be known: a time scale t_0, a length scale x_0, and a density scale ρ_0. Then the following dimensionless variables may be defined:

$$\tilde{t} = \frac{t}{t_0}, \qquad \tilde{\mathbf{x}} = \frac{\mathbf{x}}{x_0}, \qquad \tilde{\rho} = \frac{\rho}{\rho_0}. \tag{2.3}$$

It is natural to scale the velocity by $u_0 = x_0/t_0$ and the pressure by $p_0 = p(\rho_0)$, and also to define $a_0^2 = p'(\rho_0)$ and the Mach number $M = u_0/a_0$. If the corresponding dimensionless variables are used instead of the original ones, the following system is obtained:

$$\begin{cases} \partial_{\tilde{t}}\tilde{\rho} + \nabla_{\tilde{\mathbf{x}}}\cdot(\tilde{\rho}\tilde{\mathbf{u}}) = 0, \\ \partial_{\tilde{t}}(\tilde{\rho}\tilde{\mathbf{u}}) + \nabla_{\tilde{\mathbf{x}}}\cdot(\tilde{\rho}\tilde{\mathbf{u}}\otimes\tilde{\mathbf{u}}) + \dfrac{1}{\gamma M^2}\nabla_{\tilde{\mathbf{x}}}\tilde{p} = 0, \end{cases} \tag{2.4}$$

with $\tilde{\mathbf{u}} = \mathbf{u}/u_0$, $\tilde{p} = p/p_0$, and $\tilde{p}(\tilde{\rho}) := p(\rho_0\tilde{\rho})/p_0$. The coefficient γ is defined as

$$\gamma = \frac{\rho_0 a_0^2}{p_0} = \tilde{p}'(1).$$

We assume that the initial condition and the boundary condition are well prepared [27, p.631] in the sense that

$$\begin{cases} \tilde{\rho}(\tilde{\mathbf{x}}, \tilde{t}=0, M) = \tilde{\rho}_0^{(0)} + \mathcal{O}\left(M^2\right), \\ \tilde{\mathbf{u}}(\tilde{\mathbf{x}}, \tilde{t}=0, M) = \tilde{\mathbf{u}}_0^{(0)}(\tilde{\mathbf{x}}) + \mathcal{O}\left(M\right), \end{cases} \qquad \text{where} \qquad \begin{cases} \tilde{\rho}^{(0)}(\tilde{\mathbf{x}}) = \tilde{\rho}_0^{(0)} \in \mathbb{R}^+, \\ \nabla_{\tilde{\mathbf{x}}}\cdot(\tilde{\mathbf{u}}_0^{(0)}) = 0, \end{cases} \tag{2.5a}$$

and the values ρ_b and $\mathbf{u}_b$ satisfy

$$\tilde{\rho}_b(\tilde{\mathbf{x}}, \tilde{t}, M) = \tilde{\rho}_b^{(0)} + \mathcal{O}\left(M^2\right), \tag{2.5b}$$

and

$$\tilde{\mathbf{u}}_b(\tilde{\mathbf{x}}, \tilde{t}, M) = \tilde{\mathbf{u}}_b^{(0)}(\tilde{\mathbf{x}}) + \mathcal{O}\left(M\right), \qquad \text{where} \qquad \int_{\partial\Omega}\mathbf{u}_b^{(0)}\cdot\mathbf{n} = 0. \tag{2.5c}$$

We now perform a two time scales asymptotic expansion as in [29, 25]. The two time scales are the material time scale $\tilde{t}$ and the acoustic time scale $\tau = \tilde{t}/M$. Writing $\tilde{\varphi} \in \{\tilde{\rho}, \tilde{\rho}\tilde{\mathbf{u}}\}$ as an expansion of the Mach number M,

$$\tilde{\varphi}(\tilde{\mathbf{x}}, \tilde{t}; M) = \sum_{n=0}^{N} M^n\tilde{\varphi}^{(n)}(\tilde{\mathbf{x}}, \tilde{t}, \tau) + \mathcal{O}\left(M^{N+1}\right), \tag{2.6}$$

and injecting (2.6) in (2.4), it can be proven that $\tilde{\rho}^{(0)}$ does not depend on τ and $\tilde{\mathbf{x}}$, but only on $\tilde{t}$. Provided $\tilde{\rho}_b^{(0)}$ is constant, the following system coupling $\tilde{\rho}^{(1)}$ and $(\tilde{\rho}\tilde{\mathbf{u}})^{(0)}$ holds:

$$\begin{cases} \partial_\tau\tilde{\rho}^{(1)} + \nabla_{\tilde{\mathbf{x}}}\cdot(\tilde{\rho}\tilde{\mathbf{u}})^{(0)} = 0, \\ \partial_\tau\left(\tilde{\rho}\tilde{\mathbf{u}}\right)^{(0)} + \tilde{a}^2\left(\tilde{\rho}^{(0)}\right)\nabla_{\tilde{\mathbf{x}}}\tilde{\rho}^{(1)} = 0. \end{cases} \tag{2.7}$$

The system (2.7) belongs to the larger family of first order waves systems, which reads

$$\left\{\begin{array}{l} \partial_\tau \widehat{p} + \dfrac{1}{\widehat{\rho_0}} \mathrm{div}_{\mathbf{x}} \widehat{\mathbf{u}} = 0, \\ \partial_\tau \widehat{\mathbf{u}} + \widehat{\kappa_0} \nabla \widehat{p} = 0, \end{array}\right. \tag{2.8}$$

depending on two strictly nonnegative parameters, $\widehat{\kappa_0}$ and $\widehat{\rho_0}$. The wave velocity is $\widehat{c_0}$, linked with the parameters of the system by $\widehat{c_0}^2 = \widehat{\kappa_0}/\widehat{\rho_0}$. In particular, we note that system (2.7) can be written as system (2.8) with $(\widehat{p}, \widehat{\mathbf{u}}) = (\tilde{\rho}^{(1)}, (\tilde{\rho}\tilde{\mathbf{u}})^{(0)})$, $\widehat{\rho_0} = 1$ and $\widehat{\kappa_0} = \tilde{a}^2(\tilde{\rho}^{(0)})$ such that $\widehat{c_0} = \tilde{a}(\tilde{\rho}^{(0)})$. Since the initial and boundary conditions are *well prepared* (2.5), equations (2.2)–(2.5) lead us to study system (2.8) with the initial condition

$$\left\{\begin{array}{l} \widehat{p}(\mathbf{x}, \tau = 0) = 0, \\ \widehat{\mathbf{u}}(\mathbf{x}, \tau = 0) = \widehat{\mathbf{u}}_0(\mathbf{x}), \end{array}\right. \qquad \text{where} \qquad \mathrm{div}_{\mathbf{x}} \widehat{\mathbf{u}}_0 = 0, \tag{2.9a}$$

and with the boundary fluxes

$$\left[\begin{array}{c} \dfrac{1}{\widehat{\rho_0}} \widehat{\mathbf{u}} \cdot \mathbf{n} \\ \widehat{\kappa_0} \widehat{p} \mathbf{n} \end{array}\right]_{\text{wall}} = \left(\begin{array}{c} 0 \\ \widehat{\kappa_0} \widehat{p} \mathbf{n} + \widehat{c_0} (\widehat{\mathbf{u}} \cdot \mathbf{n}) \mathbf{n} \end{array}\right) \tag{2.9b}$$

for the wall boundary condition and

$$\left[\begin{array}{c} \dfrac{1}{\widehat{\rho_0}} \widehat{\mathbf{u}} \cdot \mathbf{n} \\ \widehat{\kappa_0} \widehat{p} \mathbf{n} \end{array}\right]_{\text{SW}} = \left(\begin{array}{c} \dfrac{1}{\widehat{\rho_0}} \dfrac{\widehat{\mathbf{u}} \cdot \mathbf{n} + \widehat{\mathbf{u}}_b \cdot \mathbf{n}}{2} + \dfrac{\widehat{c_0}}{2} (\widehat{p} - 0) \\ \widehat{\kappa_0} \dfrac{\widehat{p} + 0}{2} \mathbf{n} + \dfrac{\widehat{c_0}}{2} (\widehat{\mathbf{u}} \cdot \mathbf{n} - \widehat{\mathbf{u}}_b \cdot \mathbf{n}) \mathbf{n} \end{array}\right) \tag{2.9c}$$

for the inlet/outlet boundary condition.

2.2. Formal link with the long time limit of the wave system. We recall the link between the long time limit of (2.7) and the low Mach number limit problem, which was proven in [35] on unbounded domains, and which was formally done in the bounded case in [25].

As we are interested in the limit when $M \to 0$, and considering that $\tau = \tilde{t}/M$, it is natural to be interested in the long time limit of (2.8) with initial and boundary conditions given by (2.9). If this long time limit exists and is denoted by $(\widehat{p}^\infty, \widehat{\mathbf{u}}^\infty)$, we formally get

$$\begin{aligned} \tilde{\rho}(\tilde{\mathbf{x}}, \tilde{t}) &= \tilde{\rho}^{(0)} + \widehat{p}^\infty M + \mathcal{O}\left(M^2\right), \\ \tilde{\rho}\tilde{\mathbf{u}}(\tilde{\mathbf{x}}, \tilde{t}) &= \widehat{\mathbf{u}}^\infty + \mathcal{O}\left(M\right). \end{aligned}$$

The key point of the study of the existence and the characterization of the long time limit is an adapted Hodge–Helmholtz decomposition of the long time limit of the wave system. It was proven in [25] that under regularity conditions on Ω any $\mathbf{u} \in (L^2(\Omega))^d$ can be uniquely decomposed as

$$\begin{cases} \mathbf{u} = \mathbf{u}_\varphi + \mathbf{u}_{\boldsymbol{\Psi}} & \text{in } \Omega \\ \mathbf{u}_\varphi \cdot \mathbf{n} = \mathbf{u} \cdot \mathbf{n} - \mathbf{u}_b \cdot \mathbf{n} & \text{in } \partial\Omega \end{cases} \tag{2.10}$$

where $\mathbf{u}_\varphi = \nabla_{\mathbf{x}} \varphi$, $\mathbf{u}_{\boldsymbol{\Psi}} = \mathbf{u} - \nabla_{\mathbf{x}} \varphi$ and φ is solution of the following variational formulation:

$$\text{Find } \varphi \in H^1(\Omega) \quad \forall g \in H^1(\Omega) \qquad \int_\Omega \nabla_{\mathbf{x}} g \cdot \nabla_{\mathbf{x}} \varphi = \int_\Omega \mathbf{u} \cdot \nabla_{\mathbf{x}} g - \int_{\partial\Omega} g \mathbf{u}_b \cdot \mathbf{n}.$$

Using this formulation, we directly obtain that $\mathrm{div}_{\mathbf{x}}(\mathbf{u}_{\boldsymbol{\Psi}}) = 0$ in Ω and $\mathbf{u}_{\boldsymbol{\Psi}} \cdot \mathbf{n} = \mathbf{u}_b \cdot \mathbf{n}$ in $\partial\Omega$.

Using this decomposition, it was proven in [25] that the long time limit of the wave system (2.8) with initial condition $(\widehat{p}_0, \widehat{\mathbf{u}}_0)$ and with boundary conditions (2.9b)–(2.9c) exists and is given by

$$\left(\begin{array}{c} p^\infty \\ \mathbf{u}^\infty \end{array}\right) = \left(\begin{array}{c} 0 \\ \widehat{\mathbf{u}}_{\boldsymbol{\Psi}}(\widehat{\mathbf{u}}_0) \end{array}\right), \tag{2.11}$$

where $\widehat{\mathbf{u}}_{\boldsymbol{\Psi}}(\widehat{\mathbf{u}}_0)$ is the divergence-free component of the Hodge–Helmholtz decomposition (2.10) of the initial condition $\widehat{\mathbf{u}}_0$ (see [25, Appendix B] for details). The fact that the long time pressure is zero can be rewritten as $\tilde{\rho}^{(1)} = 0$, so that

$$\tilde{\rho}(\tilde{\mathbf{x}}, \tilde{t}) = \tilde{\rho}^{(0)} + \mathcal{O}\left(M^2\right),$$

which means that the pressure fluctuations should scale as M^2. Concerning the velocity, we get that

$$\tilde{\rho}\tilde{\mathbf{u}}(\tilde{\mathbf{x}},\tilde{t}) = \widehat{\mathbf{u}}_{\mathbf{\Psi}}\left((\tilde{\rho}\tilde{\mathbf{u}})_0^{(0)}\right) + \mathcal{O}(M)$$

with $\mathrm{div}_{\mathbf{x}}(\widehat{\mathbf{u}}_{\mathbf{\Psi}}) = 0$, which means that the divergence should scale as M. Note that, compared to a single scale approach, this two time scales approach allows us to really identify $(\tilde{\rho}\tilde{\mathbf{u}})^{(0)}$ as the divergence free component (with respect to Hodge–Helmholtz decomposition (2.10)) of the initial momentum field.

3. The numerical scheme and its asymptotic expansion in the low Mach number limit.

3.1. Discontinuous Galerkin discretization. For simplifying the notation, the dimensionless isentropic Euler system is briefly noted as

$$\partial_t \mathbf{W} + \nabla \cdot \mathbf{f}(\mathbf{W}) = 0, \tag{3.1}$$

where $\mathbf{W} = (\tilde{\rho}, \tilde{\rho}\tilde{\mathbf{u}})^T$ is the vector of conservative variables and $\mathbf{f}$ is the flux defined as

$$\mathbf{f}(\mathbf{W}) = \begin{pmatrix} \tilde{\rho}\tilde{\mathbf{u}} \\ \tilde{\rho}\tilde{\mathbf{u}} \otimes \tilde{\mathbf{u}} + \dfrac{1}{\gamma M^2}\,\tilde{p}\mathrm{I} \end{pmatrix}.$$

We denote by $\mathcal{M}_h$ a conformal mesh. We denote by $\mathcal{C}$ the set of cells of $\mathcal{M}_h$, $\mathcal{S}_i$ the set of interior sides of $\mathcal{M}_h$, and by $\mathcal{S}_b$ the set of boundary sides. Boundary sides are supposed to be oriented such that the normal is outgoing. Each interior side S is arbitrarily oriented, and denoting by $\mathbf{n}_S$ its normal, we will call the left cell the one from which $\mathbf{n}_S$ is outgoing and the right cell the one in which $\mathbf{n}_S$ is ingoing. We denote by V_h a finite element basis that is composed of piecewise polynomial functions. For each $\varphi \in V_h$, and along any interior side S, we denote by

$$\forall \mathbf{x} \in S, \qquad [\![\, \varphi(\mathbf{x}) \,]\!] = \varphi^{Left}(\mathbf{x}) - \varphi^{Right}(\mathbf{x}),$$

and

$$\forall \mathbf{x} \in S, \qquad \{\!\{\, \varphi(\mathbf{x}) \,\}\!\} = \frac{\varphi^{Right}(\mathbf{x}) + \varphi^{Left}(\mathbf{x})}{2}.$$

Last, we denote by $\mathcal{V}_h = (V_h)^d$ the finite element space of velocities and by $\mathbb{V}_h = (V_h)^{d+1}$ the finite element space in which the numerical solutions of (2.4) will be searched. Then the discontinuous Galerkin formulation for (3.1) is

$$\begin{aligned} \text{Find } \mathbf{W}_h \in \mathbb{V}_h \quad \forall \boldsymbol{\varphi} \in \mathbb{V}_h \qquad & \sum_{K\in\mathcal{C}} \int_K (\boldsymbol{\varphi}\partial_t \mathbf{W}_h - \mathbf{f}(\mathbf{W}_h)\cdot\nabla\boldsymbol{\varphi}) \\ + \sum_{S\in\mathcal{S}_i} \int_S [\![\, \boldsymbol{\varphi} \,]\!] \cdot \{\!\{\, \mathbf{f}(\mathbf{W}_h)\cdot\mathbf{n}_S \,\}\!\} & + \sum_{S\in\mathcal{S}_b} \int_S \boldsymbol{\varphi}^{Left} \cdot \mathbf{f}^b(\mathbf{W}_h)\cdot\mathbf{n}_S = 0, \end{aligned}$$

where $\mathbf{f}^b$ matches with the weak imposition of the boundary conditions (2.2). In the previous formulation, the flux on the sides is centered, and this formulation is known to be unstable. For recovering stability, this centered flux must be replaced by a numerical flux $\widehat{\mathbf{f}}(\mathbf{W}_h, \mathbf{n}_S)$, which gives the following numerical scheme:

$$\begin{aligned} \text{Find } \mathbf{W}_h \in \mathbb{V}_h \quad \forall \boldsymbol{\varphi} \in \mathbb{V}_h \qquad & \sum_{K\in\mathcal{C}} \int_K (\boldsymbol{\varphi}\cdot\partial_t \mathbf{W}_h - \mathbf{f}(\mathbf{W}_h)\cdot\nabla\boldsymbol{\varphi}) \\ + \sum_{S\in\mathcal{S}_i} \int_S [\![\, \boldsymbol{\varphi} \,]\!] \cdot \widehat{\mathbf{f}}(\mathbf{W}_h, \mathbf{n}_S) & + \sum_{S\in\mathcal{S}_b} \int_S \boldsymbol{\varphi}^{Left} \cdot \mathbf{f}^b(\mathbf{W}_h)\cdot\mathbf{n}_S = 0. \end{aligned} \tag{3.2}$$

The numerical flux $\widehat{\mathbf{f}}(\mathbf{W}_h, \mathbf{n}_S)$ may be any known numerical flux [38]: Roe, Lax–Friedrich, HLL, HLLC, exact Godunov, etc. For the purpose of notation, we will also denote by $\widehat{\mathbf{f}}(\mathbf{W}_L, \mathbf{W}_R, \mathbf{n}_S)$ the numerical flux acting on $\mathbb{R}^{d+1}\times\mathbb{R}^{d+1}\times\mathbb{R}^d$.

We denote by an index $[\rho]$ (resp., $[\rho\mathbf{u}]$) the mass (resp., momentum) component of the numerical flux and boundary flux. Then the numerical scheme (3.2) can be expanded equation by equation as

follows:

$$
\begin{aligned}
&\text{Find} \quad \tilde{\rho}_h \in V_h, (\tilde{\rho}\tilde{\mathbf{u}})_h \in \mathcal{V}_h \quad \text{such that} \quad \forall \varphi \in V_h, \boldsymbol{\psi} \in \mathcal{V}_h \\
&\sum_{K\in\mathcal{C}} \int_K (\varphi \cdot \partial_t \tilde{\rho}_h - (\tilde{\rho}\tilde{\mathbf{u}})_h \cdot \nabla\varphi) \\
&\qquad + \sum_{S\in\mathcal{S}_i} \int_S [\![\varphi]\!] \widehat{\mathbf{f}}_{[\rho]}(\mathbf{W}_h, \mathbf{n}_S) + \sum_{S\in\mathcal{S}_b} \int_S \varphi^{Left} \mathbf{f}^b_{[\rho]}(\mathbf{W}_h) \cdot \mathbf{n}_S = 0, \qquad (3.3a) \\
&\sum_{K\in\mathcal{C}} \int_K \left(\boldsymbol{\psi} \cdot \partial_t \left(\tilde{\rho}\tilde{\mathbf{u}}\right)_h - \frac{(\tilde{\rho}\tilde{\mathbf{u}})_h \otimes (\tilde{\rho}\tilde{\mathbf{u}})_h}{\tilde{\rho}_h} \cdot \nabla\boldsymbol{\psi} - \frac{\tilde{p}\left(\tilde{\rho}_h\right)}{\gamma M^2} \nabla_{\tilde{\mathbf{x}}} \cdot \boldsymbol{\psi} \right) \\
&\qquad + \sum_{S\in\mathcal{S}_i} \int_S [\![\boldsymbol{\psi}]\!] \cdot \widehat{\mathbf{f}}_{[\rho\mathbf{u}]}(\mathbf{W}_h, \mathbf{n}_S) + \sum_{S\in\mathcal{S}_b} \int_S \boldsymbol{\psi}^{Left} \cdot \mathbf{f}^b_{[\rho\mathbf{u}]}(\mathbf{W}_h) \cdot \mathbf{n}_S = 0. \qquad (3.3b)
\end{aligned}
$$

At a discrete level, a numerical scheme is usually considered as accurate at low Mach number provided $\tilde{p}^{(1)} = 0$ and a discrete version of the zero divergence of the velocity holds. This can be proven by analyzing the first terms of an asymptotic expansion in the Mach number M of the numerical scheme (3.3), which will be done in the following section.

3.2. Asymptotic expansion of the numerical scheme. We perform the following expansion:

$$\mathbf{W}_h = \mathbf{W}_h^{(0)} + M\mathbf{W}_h^{(1)} + M^2\mathbf{W}_h^{(2)} + \mathcal{O}\left(M^3\right)$$

where $\mathbf{W}_h^{(i)} \in \mathbb{V}_h$. This expansion can be obtained by expansion of each of the values on the degrees of freedom on a Lagrange basis of $\mathbb{V}_h$. Note that the choice of a Lagrange basis is just driven by the fact that the scale of the degrees of freedom are the same as the one of the approximated functions, thus allowing to perform a low Mach number asymptotic expansion either on the functions or on the degrees of freedom without any ambiguity. At the end, like a lot of discontinuous Galerkin methods, the numerical method does not depend on the choice of the basis.

3.2.1. Uniformity of $\tilde{\rho}^{(0)}$ and $\tilde{p}^{(0)}$.

PROPOSITION 1 (uniformity of $\tilde{\rho}^{(0)}$ and $\tilde{p}^{(0)}$).

- *If the numerical flux ensures*

$$\widehat{\mathbf{f}}(\mathbf{W}_L, \mathbf{W}_R, \mathbf{n}_S, M) = \begin{pmatrix} \frac{1}{M}\,\tilde{\alpha}\left(\tilde{\rho}_L^{(0)}, \tilde{\rho}_R^{(0)}\right)\left(\tilde{\rho}_L^{(0)} - \tilde{\rho}_R^{(0)}\right) + \mathcal{O}(1) \\ \frac{1}{M^2}\,\frac{\left(\tilde{p}_L^{(0)} + \tilde{p}_R^{(0)}\right)\mathbf{n}_S}{2\gamma} + \mathcal{O}\left(\frac{1}{M}\right) \end{pmatrix}$$

  where $\tilde{\alpha}\left(\tilde{\rho}_L^{(0)}, \tilde{\rho}_R^{(0)}\right)$ is strictly nonnegative,
- *if the wall boundary flux ensures*

$$\mathbf{f}^{wall}(\mathbf{W}_L, \mathbf{n}_S, M) = \begin{pmatrix} 0 \\ \frac{1}{\gamma M^2}\,\tilde{p}_L^{(0)}\mathbf{n}_S + \mathcal{O}\left(\frac{1}{M}\right) \end{pmatrix},$$

- *if the imposed boundary value $\tilde{\rho}_b^{(0)}$ on Steger–Warming boundary conditions is constant and uniform,*
- *if the Steger–Warming boundary flux ensures*

$$\mathbf{f}^{SW}(\mathbf{W}_L, \mathbf{W}_b, \mathbf{n}_S, M) = \begin{pmatrix} \frac{1}{M}\,\tilde{\beta}\left(\tilde{\rho}_L^{(0)}, \tilde{\rho}_b^{(0)}\right)\left(\tilde{\rho}_L^{(0)} - \tilde{\rho}_b^{(0)}\right) + \mathcal{O}(1) \\ \frac{1}{M^2}\,\frac{\left(\tilde{p}_L^{(0)} + \tilde{p}_b^{(0)}\right)\mathbf{n}_S}{2\gamma} + \mathcal{O}\left(\frac{1}{M}\right) \end{pmatrix},$$

  where $\tilde{\beta}\left(\tilde{\rho}_L^{(0)}, \tilde{\rho}_b^{(0)}\right)$ is strictly nonnegative,

then $\tilde{\rho}_h^{(0)}$ is uniform, equal to $\tilde{\rho}_b^{(0)}$.

Proof. Considering the hypothesis on the numerical flux, the numerical scheme at order $1/M$ for (3.3a) gives

$$\forall \varphi \in V_h \qquad \sum_{S\in\mathcal{S}_i}\int_S [\![\, \varphi \,]\!]\tilde{\alpha}\left(\tilde{\rho}_{h,L}^{(0)},\tilde{\rho}_{h,R}^{(0)}\right)\left(\tilde{\rho}_{h,L}^{(0)}-\tilde{\rho}_{h,R}^{(0)}\right)+\sum_{S\in\mathcal{S}_b}\int_S \varphi^L\tilde{\beta}\left(\tilde{\rho}_{h,L}^{(0)},\tilde{\rho}_b^{(0)}\right)\left(\tilde{\rho}_{h,L}^{(0)}-\tilde{\rho}_b^{(0)}\right)=0,$$

and the numerical scheme at order $1/M^2$ for (3.3b) gives

$$\forall \boldsymbol{\psi} \in \mathcal{V}_h \qquad -\sum_{K\in\mathcal{C}}\int_K \tilde{p}_h^{(0)}\nabla_{\tilde{\mathbf{x}}}\cdot\boldsymbol{\psi}+\sum_{S\in\mathcal{S}_i}\int_S [\![\, \boldsymbol{\psi} \,]\!]\cdot\left\{\!\!\left\{ \tilde{p}_h^{(0)}\mathbf{n}_S \right\}\!\!\right\}+\sum_{S\in\mathcal{S}_b}\int_S \boldsymbol{\psi}^L\cdot\left\{\!\!\left\{ \tilde{p}_h^{(0)}\mathbf{n}_S \right\}\!\!\right\}=0, \tag{3.4}$$

with the convention that on a Steger–Warming boundary condition

$$\left\{\!\!\left\{ \tilde{p}^{(0)} \right\}\!\!\right\}=\frac{\tilde{p}^{(0)}+\tilde{p}_b^{(0)}}{2},$$

whereas on a wall boundary condition

$$\left\{\!\!\left\{ \tilde{p}^{(0)} \right\}\!\!\right\}=\tilde{p}^{(0)}.$$

As the uniform solution equal to $\tilde{p}_b^{(0)}$ is a solution of (3.4),

$$\forall \boldsymbol{\psi} \in \mathcal{V}_h \qquad -\sum_{K\in\mathcal{C}}\int_K \tilde{p}_b^{(0)}\nabla_{\tilde{\mathbf{x}}}\cdot\boldsymbol{\psi}+\sum_{S\in\mathcal{S}_i}\int_S [\![\, \boldsymbol{\psi} \,]\!]\cdot\left\{\!\!\left\{ \tilde{p}_b^{(0)}\mathbf{n}_S \right\}\!\!\right\}+\sum_{S\in\mathcal{S}_b}\int_S \boldsymbol{\psi}^L\cdot\left\{\!\!\left\{ \tilde{p}_b^{(0)}\mathbf{n}_S \right\}\!\!\right\}=0.$$

This last equation can be withdrawn from (3.4) for finding

$$\begin{aligned}\forall \boldsymbol{\psi} \in \mathcal{V}_h \qquad &-\sum_{K\in\mathcal{C}}\int_K \left(\tilde{p}_h^{(0)}-\tilde{p}_b^{(0)}\right)\nabla_{\tilde{\mathbf{x}}}\cdot\boldsymbol{\psi}+\sum_{S\in\mathcal{S}_i}\int_S [\![\, \boldsymbol{\psi} \,]\!]\cdot\left\{\!\!\left\{ \left(\tilde{p}_h^{(0)}-\tilde{p}_b^{(0)}\right)\mathbf{n}_S \right\}\!\!\right\}\\ &+\sum_{S\in\mathcal{S}_b}\int_S \boldsymbol{\psi}^L\cdot\left\{\!\!\left\{ \left(\tilde{p}_h^{(0)}-\tilde{p}_b^{(0)}\right)\mathbf{n}_S \right\}\!\!\right\}=0.\end{aligned}$$

A simple integration by part on each cell gives

$$\forall \boldsymbol{\psi} \in \mathcal{V}_h \quad \forall K \in \mathcal{C} \qquad \int_K \boldsymbol{\psi}\cdot\nabla_{\tilde{\mathbf{x}}}\left(\tilde{p}_h^{(0)}-\tilde{p}_b^{(0)}\right)=0,$$

which means that $\nabla_{\tilde{\mathbf{x}}}\tilde{p}_h^{(0)}=0$ on all cells, so that $\tilde{p}_h^{(0)}$ is piecewise constant, and so is $\tilde{\rho}_h^{(0)}$. Then following the result for a finite volume scheme [25], this gives $\tilde{\rho}_h^{(0)}$ uniform, equal to $\tilde{\rho}_b^{(0)}$. As a consequence, $\tilde{p}_h^{(0)}$ is also uniform, equal to $p\left(\tilde{\rho}_b^{(0)}\right)$. ∎

3.2.2. Asymptotic consistency with the discrete wave system. The semidiscrete discontinuous Galerkin method for the wave system (2.8) reads

$$\begin{cases}\displaystyle\sum_{K\in\mathcal{C}}\int_K \varphi\partial_\tau\widehat{p}_h-\sum_{K\in\mathcal{C}}\int_K \frac{1}{\widehat{\rho_0}}\,\widehat{\mathbf{u}}_h\cdot\nabla\varphi+\sum_{S\in\mathcal{S}_i}\int_S [\![\, \varphi \,]\!]\left(\frac{1}{\widehat{\rho_0}}\,\{\!\{\widehat{\mathbf{u}}_h\cdot\mathbf{n}_S\}\!\}-d_{11}\,[\![\, \widehat{p}_h \,]\!]\right)\\ \qquad\qquad\qquad\qquad\qquad\qquad\qquad\qquad\qquad\qquad\qquad\qquad\qquad\qquad+\displaystyle\sum_{S\in\mathcal{S}_b}\int_S \varphi^L\left[\frac{1}{\widehat{\rho}_0}\widehat{\mathbf{u}}_h\cdot\mathbf{n}_S\right]_b=0,\\ \displaystyle\sum_{K\in\mathcal{C}}\int_K \boldsymbol{\psi}\cdot\partial_\tau\widehat{\mathbf{u}}_h-\sum_{K\in\mathcal{C}}\int_K \widehat{\kappa_0}\widehat{p}_h\mathrm{div}_{\mathbf{x}}\boldsymbol{\psi}+\sum_{S\in\mathcal{S}_i}\int_S [\![\, \boldsymbol{\psi} \,]\!]\cdot\left(\widehat{\kappa_0}\,\{\!\{\widehat{p}_h\mathbf{n}_S\}\!\}-[\![\, \mathbf{D}_{22}(\mathbf{n}_S)\widehat{\mathbf{u}}_h \,]\!]\right)\\ \qquad\qquad\qquad\qquad\qquad\qquad\qquad\qquad\qquad\qquad\qquad\qquad\qquad\qquad+\displaystyle\sum_{S\in\mathcal{S}_b}\int_S \boldsymbol{\psi}^L\left[\widehat{\kappa_0}\widehat{p}_h\cdot\mathbf{n}_S\right]_b=0,\end{cases} \tag{3.5}$$

where

$$\mathbf{D}(\mathbf{n})=\begin{pmatrix} d_{11} & 0\\ 0 & \mathbf{D}_{22}(\mathbf{n})\end{pmatrix}. \tag{3.6}$$

matches with the stabilization matrix and the boundary fluxes are given by (2.9b) for wall boundary condition and (2.9c) for inlet/outlet boundary condition. We recall that Godunov stabilization is given by

$$\mathbf{D}^{\mathrm{Godunov}}(\mathbf{n})=\frac{\widehat{c_0}}{2}\begin{pmatrix} 1 & 0\\ 0 & \mathbf{n}\mathbf{n}^T\end{pmatrix}, \tag{3.7}$$

while Rusanov stabilization is given by

$$\mathbf{D}^{\text{Rusanov}}(\mathbf{n}) = \frac{\widehat{c_0}}{2}\begin{pmatrix} 1 & 0 \\ 0 & \mathrm{I}_d \end{pmatrix}. \tag{3.8}$$

We now state the link between the discretization (3.3) of (3.1) and the discretization (3.5) of the wave system (2.8).

PROPOSITION 2 (consistency with the wave system). *We assume that the hypothesis of Proposition 1 holds, so that* $\tilde{\rho}_h^{(0)} = \tilde{\rho}_b^{(0)}$ *and we denote by*

$$\tilde{\alpha}_b^{(0)} := \tilde{\alpha}\left(\tilde{\rho}_b^{(0)}, \tilde{\rho}_b^{(0)}\right), \qquad \tilde{a}_b^{(0)} := \tilde{a}\left(\tilde{\rho}_b^{(0)}\right).$$

Moreover, we suppose that the numerical flux ensures the asymptotic development (once $\tilde{\rho}_h^{(0)} = \tilde{\rho}_b^{(0)}$ *is ensured)*

$$\widehat{\mathbf{f}}(\mathbf{W}_L, \mathbf{W}_R, \mathbf{n}, M) = \begin{pmatrix} \dfrac{\left((\tilde{\rho}\tilde{\mathbf{u}})_L^{(0)} + (\tilde{\rho}\tilde{\mathbf{u}})_R^{(0)}\right)\cdot\mathbf{n}}{2} + \tilde{\alpha}_b^{(0)}\left(\tilde{\rho}_L^{(1)} - \tilde{\rho}_R^{(1)}\right) + \mathcal{O}(M) \\ \dfrac{1}{M}\left(\dfrac{\left(\tilde{p}_L^{(1)} + \tilde{p}_R^{(1)}\right)\mathbf{n}}{2\gamma} + \mathbf{D}_{22}(\mathbf{n})\left((\tilde{\rho}\tilde{\mathbf{u}})_L^{(0)}\cdot\mathbf{n} - (\tilde{\rho}\tilde{\mathbf{u}})_R^{(0)}\right)\right) + \mathcal{O}(1) \end{pmatrix} \tag{3.9}$$

and that the boundary flux ensures the following asymptotic expansion:

- *on the wall boundary condition*

$$\mathbf{f}^{wall}_{[\tilde{\rho}\tilde{\mathbf{u}}]}(\mathbf{W}_L, \mathbf{n}, M) = \frac{1}{M}\left(\frac{\tilde{p}_L^{(1)}}{\gamma}\mathbf{n} + \tilde{a}_b^{(0)}\,\tilde{\rho}_b^{(0)}\left(\tilde{\mathbf{u}}_L^{(0)}\cdot\mathbf{n}\right)\mathbf{n}\right) + \mathcal{O}(1),$$

- *on the Steger–Warming boundary condition*

$$\mathbf{f}^{SW}(\mathbf{W}_L, \mathbf{W}_b, \mathbf{n}, M) = \begin{pmatrix} \tilde{\rho}_b^{(0)}\dfrac{\left(\tilde{\mathbf{u}}_i^{(0)} + \tilde{\mathbf{u}}_b^{(0)}\right)\cdot\mathbf{n}}{2} + \dfrac{\tilde{a}_b^{(0)}}{2}\left(\tilde{\rho}_i^{(1)} - \tilde{\rho}_b^{(1)}\right) + \mathcal{O}(M) \\ \dfrac{1}{M}\left(\left(\tilde{a}_b^{(0)}\right)^2\dfrac{\tilde{\rho}_i^{(1)} + \tilde{\rho}_b^{(1)}}{2} + \dfrac{\tilde{a}_b^{(0)}\tilde{\rho}_b^{(0)}}{2}\left(\tilde{\mathbf{u}}_i^{(0)} - \tilde{\mathbf{u}}_b^{(0)}\right)\cdot\mathbf{n}\right)\mathbf{n} + \mathcal{O}(1) \end{pmatrix};$$

then $(\tilde{\rho}_h^{(1)}, (\tilde{\rho}\tilde{\mathbf{u}})_h^{(0)})$ *follows the discretization (3.5) with* $\widehat{\rho_0} = 1$, $\widehat{\kappa_0} = \left(\tilde{a}_b^{(0)}\right)^2$ $(\widehat{c_0} = \tilde{a}_b^{(0)})$, *and with the numerical dissipation (3.6) given by*

$$\mathbf{D}(\mathbf{n}) = \begin{pmatrix} \tilde{\alpha}_b^{(0)} & 0 \\ 0 & \mathbf{D}_{22}(\mathbf{n}) \end{pmatrix}. \tag{3.10}$$

Proof. The proof is similar to the proof done for the finite volume case [25]. ∎

4. Accuracy of the high order discontinuous Galerkin method on simplicial meshes with a contact preserving flux.

4.1. Statement of the main results.

We first define a discrete gradient and a discrete divergence by using the derivative in the sense of distributions.

DEFINITION 4.1 (discrete gradient). *The discrete gradient* $\nabla^{\mathcal{M}_h}$ *is defined as*

$$\nabla^{\mathcal{M}_h} : V_h \longmapsto \left(L^2(\mathcal{C})\right)^d \times \left(L^2(\mathcal{S})\right)^d,$$

such that

- $\forall p_h \in V_h$, $\forall K \in \mathcal{C}$, $\forall \mathbf{x} \in K$

$$\left(\nabla^{\mathcal{M}_h} p_h\right)\big|_K(\mathbf{x}) = \nabla\left(p_h|_K\right)(\mathbf{x}),$$

- $\forall p_h \in V_h$, $\forall S \in \mathcal{S}$, $\forall \mathbf{x} \in S$

$$\left(\nabla^{\mathcal{M}_h} p_h\right)\big|_S(\mathbf{x}) = [\![p_h(\mathbf{x})]\!]\, \mathbf{n}_S = \left(p_h|_{Left}(\mathbf{x}) - p_h|_{Right}(\mathbf{x}) \right) \mathbf{n}_S$$

with the convention $[\![p_h(\mathbf{x})]\!]_{wall} = 0$ *and* $[\![p_h(\mathbf{x})]\!]_{SW} = p_h(\mathbf{x}) - p_b$.

From a practical point of view, considering $p_h \in V_h$, it can be written on each cell K as

$$\forall \mathbf{x} \in K, \qquad p_h|_K(x) = \sum_{i=1}^{N} p_i^K \varphi_i^K(\mathbf{x}),$$

where $(\varphi_i^K)_{1 \leqslant i \leqslant N}$ are the basis functions on cell K. The discrete gradient of p_h on cell K is then given by

$$\forall \mathbf{x} \in K, \qquad \left(\nabla^{\mathcal{M}_h} p_h\right)\big|_K(\mathbf{x}) = \sum_{i=1}^{N} p_i^K \nabla \varphi_i^K(\mathbf{x}).$$

If the approximation space is composed of the piecewise two-dimensional polynomial of degree k, the cell component is composed of a two-dimensional polynomial of degree $k-1$ per cell, whereas the face component is composed of a piecewise one-dimensional polynomial of degree k per face.

DEFINITION 4.2 (discrete divergence). *The discrete divergence* $\mathrm{div}_{\mathbf{x}}^{\mathcal{M}_h}$ *is defined as*

$$\mathrm{div}_{\mathbf{x}}^{\mathcal{M}_h} : \mathcal{V}_h \longmapsto L^2(\mathcal{C}) \times L^2(\mathcal{S}),$$

such that

- $\forall \mathbf{u}_h \in \mathcal{V}_h$, $\forall K \in \mathcal{C}$, $\forall \mathbf{x} \in K$

$$\left(\mathrm{div}_{\mathbf{x}}^{\mathcal{M}_h} \mathbf{u}_h\right)\Big|_K(\mathbf{x}) = \mathrm{div}_{\mathbf{x}}\left(\mathbf{u}_h|_K\right)(\mathbf{x}),$$

- $\forall \mathbf{u}_h \in \mathcal{V}_h$, $\forall S \in \mathcal{S}$, $\forall \mathbf{x} \in S$

$$\left(\mathrm{div}_{\mathbf{x}}^{\mathcal{M}_h} \mathbf{u}_h\right)\Big|_S(\mathbf{x}) = [\![\mathbf{u}_h(\mathbf{x}) \cdot \mathbf{n}_S]\!] = \mathbf{u}_h|_{Left}(\mathbf{x}) \cdot \mathbf{n}_S - \mathbf{u}_h|_{Right}(\mathbf{x}) \cdot \mathbf{n}_S$$

with the convention $[\![\mathbf{u}_h(\mathbf{x}) \cdot \mathbf{n}_S]\!]_{wall} = 2\mathbf{u}_h(\mathbf{x}) \cdot \mathbf{n}_S$ *and* $[\![\mathbf{u}_h(\mathbf{x}) \cdot \mathbf{n}_S]\!]_{SW} = \mathbf{u}_h(\mathbf{x}) \cdot \mathbf{n}_S - \mathbf{u}_b(\mathbf{x}) \cdot \mathbf{n}_S$.

The aim of this section is to prove the following.

PROPOSITION 3. *Using a discretization* (3.5) *of the wave system with Godunov stabilization* (3.7)*, the long time limit* $(\widehat{p}_h, \widehat{\mathbf{u}}_h)$*, if it exists, is such that*

$$\nabla^{\mathcal{M}_h} \widehat{p}_h = 0 \qquad \textit{and} \qquad \mathrm{div}_{\mathbf{x}}^{\mathcal{M}_h} \widehat{\mathbf{u}}_h = 0.$$

COROLLARY 4.3 (low Mach number accuracy on triangles and tetrahedra). *If we assume that the hypotheses of Propositions 1 and 2 hold and that the numerical flux used for the Euler system ensures* (3.9) *where the numerical dissipation* (3.10) *matches with the Godunov stabilization* (3.7)*, then the numerical scheme is low Mach number accurate in the sense that its low Mach number limit satisfies*

$$\tilde{\rho}_h - \tilde{\rho}^{(0)} = \mathcal{O}\left(M^2\right) \qquad \textit{and} \qquad \mathrm{div}_{\mathbf{x}}^{\mathcal{M}_h}\left(\tilde{\rho}\tilde{\mathbf{u}}\right) = \mathcal{O}\left(M\right).$$

This can be rewritten

$$\nabla^{\mathcal{M}_h} \tilde{\rho}_h = \mathcal{O}\left(M^2\right), \qquad \textit{and} \qquad \mathrm{div}_{\mathbf{x}}^{\mathcal{M}_h} \tilde{\mathbf{u}}_h = \mathcal{O}\left(M\right).$$

This corollary is a direct consequence of the link between the low Mach number accuracy for the Euler system and the properties of the long time limit of the asymptotic wave system obtained in Proposition 2. Proposition 3 characterizes the long time limit of the wave system.

We note that various numerical fluxes for the Euler system ensure (3.9), where the numerical dissipation (3.10) matches with the Godunov stabilization (3.7), in particular the HLLC, Roe, Osher, Godunov, or Vijayasundaram (used in [16]) numerical flux. Some others rather match with the stabilization (3.8), such as Lax–Friedrich or HLL.

The proof of Proposition 3 is organized as follows. In subsection 4.2, some notation is introduced, and some classical results on the vector approximation space on simplices are recalled. Then in subsection 4.3, a technical proposition on the traces of the scalar and vector approximation spaces is proven. Last, in subsection 4.4, the proof of Proposition 3 is performed.

4.2. Some notation and known results on the approximation space of vectors. Following [8], for a cell K_i, we define

$$R_k(\partial K_i) = \left\{ \phi \mid \quad \phi \in L^2(\partial K_i) \qquad \text{and} \qquad \forall j \in \mathcal{N}(i) \quad \phi|_{\Gamma_{ij}} \in \mathbb{P}_k(\Gamma_{ij}) \right\}.$$

We define the velocity space of variable by

$$BDM_k = (\mathbb{P}_k(K))^d.$$

Then we denote by Tr and $\mathbf{Tr}$ the following trace operators:

$$\begin{array}{rcl} \mathrm{Tr} : p \in \mathbb{P}_k(K) & \longmapsto & p|_{\partial K} \in R_k(\partial K), \\ \mathbf{Tr} : \mathbf{u} \in BDM_k(K) & \longmapsto & \mathbf{u}|_{\partial K} \cdot \mathbf{n}_{ij} \in R_k(\partial K). \end{array}$$

For each cell K, we also define the two following sets:

$$\nabla_{\mathbf{x}}^{\perp} = \left\{ \mathbf{u} \in BDM_k \mid \quad \forall p \in \mathbb{P}_k \qquad \int_K \mathbf{u} \cdot \nabla p = 0 \right\},$$

and

$$\mathrm{div}_{\mathbf{x}}^{\perp} = \left\{ p \in \mathbb{P}_k \mid \quad \forall \mathbf{u} \in BDM_k \qquad \int_K p \mathrm{div}_{\mathbf{x}} \mathbf{u} = 0 \right\}.$$

On a simplicial cell, if d denotes the dimension, then we have $\dfrac{(k+d)!}{k!d!}$ degrees of freedom for each variable. Moreover, we have

$$\dim BDM_k = \dim(\mathbb{P}_k(K))^d = d \times \frac{(k+d)!}{k!d!} = \frac{(k+d)!}{k!(d-1)!}.$$

In dimension d, each face of the d-dimensional simplex is a simplex of dimension $d-1$ and therefore has $\dfrac{(k+d-1)!}{k!(d-1)!}$ degrees of freedom. Summing the degrees of freedom on the faces gives

$$\dim R_k(\partial K) = \frac{(k+d-1)!(d+1)}{k!(d-1)!}.$$

We recall the proposition proven in [8, Proposition 3.1]

Proposition 4 (Proposition 3.1 of [8]). *For $k \geqslant 1$ and for any $\mathbf{q} \in BDM_k(K)$, the following relations imply $\mathbf{q} = 0$:*

1. $\forall p_k \in R_k(\partial K) \qquad \displaystyle\int_{\partial K} p_k \mathbf{q} \cdot \mathbf{n} \, \mathrm{d}s = 0,$
2. $\forall p_{k-1} \in \mathbb{P}_{k-1}(K) \qquad \displaystyle\int_K \nabla p_{k-1} \cdot \mathbf{q} = 0,$
3. $\forall \boldsymbol{\phi}_k \in \Phi_k \qquad \displaystyle\int_K \mathbf{q} \cdot \boldsymbol{\phi}_k = 0$

   where Φ_k is defined as

$$\Phi_k = \left\{ \boldsymbol{\phi}_k \in (\mathbb{P}_k(K))^d \mid \quad \mathrm{div}_{\mathbf{x}} \boldsymbol{\phi}_k = 0 \quad \textit{and} \quad (\boldsymbol{\phi}_k \cdot \mathbf{n})|_{\partial K} = 0 \right\}.$$

We denote by $(\hat{f}_i)$ a basis of $R_k(\partial K)$. As the application $\mathbf{Tr}$ from BDM_k to $R_k(\partial K)$ is surjective, there exists at least one $\mathbf{f}_i \in BDM_k$ such that $\mathbf{Tr}(\mathbf{f}_i) = \hat{f}_i$. Suppose that another $\mathbf{g}$ exists such that $\mathbf{Tr}(\mathbf{g}) = \hat{f}_i$. Then

$$\forall p_k \in R_k(\partial K) \qquad \int_{\partial K} p_k \left(\mathbf{f}_i - \mathbf{g} \right) \cdot \mathbf{n}_{ij} = 0.$$

Therefore, following Proposition 4, uniqueness of $(\mathbf{f}_i)$ is recovered provided we suppose moreover that

$$\begin{cases} \forall \boldsymbol{\phi}_k \in \Phi_k \qquad \displaystyle\int_K (\mathbf{f}_i - \mathbf{g}) \cdot \boldsymbol{\phi}_k = 0, \\ \forall p_{k-1} \in \mathbb{P}_{k-1}(K) \qquad \displaystyle\int_K \nabla p_{k-1} \cdot (\mathbf{f}_i - \mathbf{g}) = 0. \end{cases}$$

Proposition 4 states that

$$BDM_k = \mathrm{span}(\mathbf{f}_i) \oplus \nabla \mathbb{P}_{k-1}(K) \oplus \Phi_k \tag{4.1}$$

where the direct sum is orthogonal for the L^2 scalar product in K.

4.3. Surjection of $\mathbf{Tr}(\nabla_{\mathbf{x}}^{\perp}) + \mathrm{Tr}(\mathrm{div}_{\mathbf{x}}^{\perp})$ in $R_k(\partial K)$. The aim of this subsection is to prove the following.

PROPOSITION 5. *If K is a simplicial cell, then*

$$R_k(\partial K) = \mathrm{Tr}(\mathrm{div}_{\mathbf{x}}^{\perp}) \oplus \mathbf{Tr}(\nabla_{\mathbf{x}}^{\perp}).$$

The proof needs three technical lemmas that we first prove.

LEMMA 4.4 (rank of the trace of $\nabla_{\mathbf{x}}^{\perp}$). *If K is a simplicial cell, then*

$$\mathrm{rank}\left(\mathbf{Tr}\left(\nabla_{\mathbf{x}}^{\perp}\right)\right) = \frac{(k+d-1)!d}{k!(d-1)!}.$$

Proof. For any $p_k \in \mathbb{P}_k(K)$, we have

$$\forall \boldsymbol{\phi} \in \Phi_k \qquad \int_K \nabla p_k \cdot \boldsymbol{\phi} = \int_K \mathrm{div}_{\mathbf{x}}(p_k \boldsymbol{\phi}) - \int_K p_k \mathrm{div}_{\mathbf{x}} \boldsymbol{\phi} = \int_{\partial K} p_k \boldsymbol{\phi} \cdot \mathbf{n} - \int_K p_k \mathrm{div}_{\mathbf{x}} \boldsymbol{\phi} = 0;$$

therefore, $\nabla p_k \in \Phi_k^{\perp} = \mathrm{span}(\mathbf{f}_i) \oplus \nabla \mathbb{P}_{k-1}(K)$, which leads to

$$\mathrm{span}(\mathbf{f}_i) + \nabla \mathbb{P}_k(K) = \mathrm{span}(\mathbf{f}_i) \oplus \nabla \mathbb{P}_{k-1}(K),$$

so that

$$\dim \mathrm{span}(\mathbf{f}_i) + \dim \nabla \mathbb{P}_{k-1}(K) = \dim \mathrm{span}(\mathbf{f}_i) + \dim \nabla \mathbb{P}_k(K) - \dim\left(\nabla \mathbb{P}_k(K) \cap \mathrm{span}(\mathbf{f}_i)\right),$$

which leads to

$$\begin{aligned}
\dim\left(\nabla \mathbb{P}_k(K) \cap \mathrm{span}(\mathbf{f}_i)\right) &= \dim \nabla \mathbb{P}_k(K) - \dim \nabla \mathbb{P}_{k-1}(K) \\
&= \frac{(k+d)!}{k!d!} - 1 - \left(\frac{(k-1+d)!}{(k-1)!d!} - 1\right) \\
&= \frac{(k-1+d)!}{k!d!}\,(k+d-k), \\
\dim\left(\nabla \mathbb{P}_k(K) \cap \mathrm{span}(\mathbf{f}_i)\right) &= \frac{(k+d-1)!}{k!(d-1)!}.
\end{aligned}$$

As $\left(\nabla_{\mathbf{x}}^{\perp} \cap \mathrm{span}(\mathbf{f}_i)\right) \subset \mathrm{span}(\mathbf{f}_i)$, this immediately gives

$$\begin{aligned}
\dim\left(\nabla_{\mathbf{x}}^{\perp} \cap \mathrm{span}(\mathbf{f}_i)\right) &= \dim \mathrm{span}(\mathbf{f}_i) - \dim\left(\nabla \mathbb{P}_k(K) \cap \mathrm{span}(\mathbf{f}_i)\right) \\
&= \dim R_k(\partial K) - \dim\left(\nabla \mathbb{P}_k(K) \cap \mathrm{span}(\mathbf{f}_i)\right) \\
&= (d+1)\,\frac{(k+d-1)!}{k!(d-1)!} - \frac{(k+d-1)!}{k!(d-1)!}, \\
\dim\left(\nabla_{\mathbf{x}}^{\perp} \cap \mathrm{span}(\mathbf{f}_i)\right) &= \frac{(k+d-1)!d}{k!(d-1)!}.
\end{aligned}$$

Let's summarize what we know on $\nabla_{\mathbf{x}}^{\perp}$. Considering (4.1), $\nabla_{\mathbf{x}}^{\perp}$ is the sum of Φ_k and $\mathrm{span}(\mathbf{f}_i) \cap \nabla_{\mathbf{x}}^{\perp}$. But the trace of Φ_k is zero. By definition, $\mathbf{Tr}$ is a bijection between $\mathrm{span}(\mathbf{f}_i)$ and $R_k(\partial K)$, so that

$$\mathrm{rank}\left(\mathbf{Tr}\left(\nabla_{\mathbf{x}}^{\perp}\right)\right) = \mathrm{rank}\left(\mathbf{Tr}\left(\nabla_{\mathbf{x}}^{\perp} \cap \mathrm{span}(\mathbf{f}_i)\right)\right) = \dim\left(\nabla_{\mathbf{x}}^{\perp} \cap \mathrm{span}(\mathbf{f}_i)\right) = \frac{(k+d-1)!d}{k!(d-1)!}.$$

LEMMA 4.5 (rank of the trace of $\mathrm{div}_{\mathbf{x}}^{\perp}$). *If K is a simplicial cell, then*

$$\mathrm{rank}\left(\mathrm{Tr}\left(\mathrm{div}_{\mathbf{x}}^{\perp}\right)\right) = \frac{(k+d-1)!}{k!(d-1)!}.$$

Proof. Any element of $\mathbb{P}_{k-1}(K)$ can be written as the divergence of an element of BDM_k. As $\mathrm{div}_{\mathbf{x}}(BDM_k) = \mathbb{P}_{k-1}(K)$, and as $\mathbb{P}_{k-1}(K) \subset P_k(K)$, then

$$\mathbb{P}_k(K) = \mathbb{P}_{k-1}(K) \oplus \mathrm{div}_{\mathbf{x}}^{\perp},$$

where the direct sum is orthogonal. We find

$$\begin{aligned}\dim\left(\mathrm{div}_{\mathbf{x}}^{\perp}\right) &= \dim\mathbb{P}_k(K) - \dim\mathbb{P}_{k-1}(K)\\ &= \frac{(k+d)!}{k!d!} - \frac{(k-1+d)!}{(k-1)!d!}\\ &= \frac{(k+d-1)!}{k!d!}\left((k+d)-k\right),\\ \dim\left(\mathrm{div}_{\mathbf{x}}^{\perp}\right) &= \frac{(k+d-1)!}{k!(d-1)!}.\end{aligned}$$

Now, we consider the application

$$\mathrm{Tr}_{|\mathrm{div}_{\mathbf{x}}^{\perp}} : p_k \in \mathrm{div}_{\mathbf{x}}^{\perp} \longmapsto \mathrm{Tr}(p_k).$$

For any p_k and $\mathbf{u} \in BDM_k$, we have

$$\int_{\partial K}\mathrm{Tr}(p_k)\mathbf{Tr}(\mathbf{u}) = \int_K \mathrm{div}_{\mathbf{x}}(p_k\mathbf{u}) = \int_K \mathbf{u}\cdot\nabla p_k + \int_K p_k\mathrm{div}_{\mathbf{x}}\mathbf{u}.$$

Suppose that $\mathrm{Tr}(p_k) = 0$ and that $p_k \in \mathrm{div}_{\mathbf{x}}^{\perp}$. Then we find

$$\forall \mathbf{u} \in BDM_k \qquad \int_K \mathbf{u}\cdot\nabla p_k = 0,$$

so that p_k is uniform on K. But as it vanishes on ∂K, $p_k = 0$. This means that $\mathrm{Tr}_{|\mathrm{div}_{\mathbf{x}}^{\perp}}$ is injective, so that using the rank-nullity theorem

$$\mathrm{rank}\left(\mathrm{Tr}\left(\mathrm{div}_{\mathbf{x}}^{\perp}\right)\right) = \dim\left(\mathrm{div}_{\mathbf{x}}^{\perp}\right) = \frac{(k+d-1)!}{k!(d-1)!}.$$

LEMMA 4.6 (direct sum of the traces). *If K is a simplicial cell, then*

$$\mathbf{Tr}(\nabla_{\mathbf{x}}^{\perp}) \cap \mathrm{Tr}(\mathrm{div}_{\mathbf{x}}^{\perp}) = \{0\}.$$

Proof. We denote by $\hat{\phi}$ an element of $R_k(\partial K)$. We suppose that $\hat{\phi}$ belongs to $\mathbf{Tr}(\nabla_{\mathbf{x}}^{\perp})$; then

$$\exists \mathbf{u} \in \nabla_{\mathbf{x}}^{\perp}, \qquad \hat{\phi} = \mathbf{Tr}(\mathbf{u}).$$

Moreover, we suppose that $\hat{\phi}$ belongs to $\mathrm{Tr}(\mathrm{div}_{\mathbf{x}}^{\perp})$; then

$$\exists p \in \mathrm{div}_{\mathbf{x}}^{\perp}, \qquad \hat{\phi} = \mathrm{Tr}(p).$$

Then we obtain

$$\begin{aligned}\int_{\partial K}\left(\hat{\phi}\right)^2 &= \int_{\partial K}\mathbf{Tr}(\mathbf{u})\mathrm{Tr}(p)\\ &= \int_K \mathrm{div}_{\mathbf{x}}(p\mathbf{u})\\ &= \int_K p\mathrm{div}_{\mathbf{x}}\mathbf{u} + \int_K \mathbf{u}\cdot\nabla p,\\ \int_{\partial K}\left(\hat{\phi}\right)^2 &= 0,\end{aligned}$$

because $p \in \mathrm{div}_{\mathbf{x}}^{\perp}$ and $\mathbf{u} \in \nabla_{\mathbf{x}}^{\perp}$. We conclude that $\hat{\phi} = 0$.

We can now use a different lemma for proving Proposition 5. It is straightforward that $\mathrm{Tr}(\mathrm{div}_{\mathbf{x}}^{\perp}) + \mathbf{Tr}(\nabla_{\mathbf{x}}^{\perp}) \subset R_k(\partial K)$. Following Theorem 4.6, the sum of $\mathbf{Tr}(\mathrm{div}_{\mathbf{x}}^{\perp})$ and $\mathrm{Tr}(\nabla_{\mathbf{x}}^{\perp})$ is direct. Then, following Theorem 4.4 and Theorem 4.5, we obtain

$$\begin{aligned}\dim\left(\mathrm{Tr}(\mathrm{div}_{\mathbf{x}}^{\perp}) \oplus \mathbf{Tr}(\nabla_{\mathbf{x}}^{\perp})\right) &= \dim\mathrm{Tr}(\mathrm{div}_{\mathbf{x}}^{\perp}) + \dim\mathbf{Tr}(\nabla_{\mathbf{x}}^{\perp})\\ &= \frac{(k+d-1)!}{k!(d-1)!} + d\,\frac{(k+d-1)!}{k!(d-1)!}\\ &= (d+1)\,\frac{(k+d-1)!}{k!(d-1)!},\\ \dim\left(\mathrm{Tr}(\mathrm{div}_{\mathbf{x}}^{\perp}) \oplus \mathbf{Tr}(\nabla_{\mathbf{x}}^{\perp})\right) &= \dim R_k(\partial K),\end{aligned}$$

which ends the proof of Proposition 5.

4.4. Proof of Proposition 3. By integrating by parts the cell integral of (3.5), we find

$$-\int_{K_i}\widehat{\mathbf{u}}\cdot\nabla\varphi=-\int_{K_i}\mathrm{div}_{\mathbf{x}}(\varphi\widehat{\mathbf{u}})+\int_{K_i}\varphi\mathrm{div}_{\mathbf{x}}\widehat{\mathbf{u}}=-\sum_{j\in\mathcal{N}(i)}\int_{\Gamma_{ij}}\varphi\widehat{\mathbf{u}}_i\cdot\mathbf{n}_{ij}+\int_{K_i}\varphi\mathrm{div}_{\mathbf{x}}\widehat{\mathbf{u}}, \tag{4.2}$$

and

$$-\int_{K_i}\widehat{p}\mathrm{div}_{\mathbf{x}}\boldsymbol{\psi}=-\int_{K_i}\mathrm{div}_{\mathbf{x}}(\boldsymbol{\psi}\widehat{p})+\int_{K_i}\boldsymbol{\psi}\cdot\nabla\widehat{p}=-\sum_{j\in\mathcal{N}(i)}\int_{\Gamma_{ij}}\widehat{p}\boldsymbol{\psi}\cdot\mathbf{n}_{ij}+\int_{K_i}\boldsymbol{\psi}\cdot\nabla\widehat{p}, \tag{4.3}$$

so that

$$\left\{\begin{array}{l}\displaystyle\int_{K_i}\varphi\partial_\tau\widehat{p}+\int_{K_i}\frac{1}{\widehat{\rho_0}}\,\varphi\mathrm{div}_{\mathbf{x}}\widehat{\mathbf{u}}+\sum_{j\in\mathcal{N}_{\mathrm{int}}(i)}\int_{\Gamma_{ij}}\frac{\varphi}{2}\left(\frac{1}{\widehat{\rho_0}}[\![\,\widehat{\mathbf{u}}\cdot\mathbf{n}_{ij}\,]\!]-2d_{11}[\![\,\widehat{p}\,]\!]\right)\\ \qquad\qquad\displaystyle+\sum_{j\in\mathcal{N}_b(i)}\int_{\Gamma_{ij}}\frac{\varphi}{2}\left(\frac{1}{\widehat{\rho_0}}[\![\,\widehat{\mathbf{u}}\cdot\mathbf{n}_{ij}\,]\!]-\widehat{c_0}[\![\,\widehat{p}\,]\!]\right)=0,\\ \displaystyle\int_{K_i}\boldsymbol{\psi}\cdot\partial_\tau\widehat{\mathbf{u}}+\int_{K_i}\widehat{\kappa_0}\boldsymbol{\psi}\cdot\nabla\widehat{p}+\sum_{j\in\mathcal{N}_{\mathrm{int}}(i)}\int_{\Gamma_{ij}}\frac{\boldsymbol{\psi}}{2}\cdot(\widehat{\kappa_0}[\![\,\widehat{p}\mathbf{n}_{ij}\,]\!]-2[\![\,\mathbf{D}_{22}(\mathbf{n}_{ij})\widehat{\mathbf{u}}\,]\!])\\ \qquad\qquad\displaystyle+\sum_{j\in\mathcal{N}_b(i)}\int_{\Gamma_{ij}}\frac{\boldsymbol{\psi}}{2}\cdot(\widehat{\kappa_0}[\![\,\widehat{p}\mathbf{n}_{ij}\,]\!]-\widehat{c_0}[\![\,\widehat{\mathbf{u}}\cdot\mathbf{n}_{ij}\,]\!])=0.\end{array}\right.$$

Using (3.7), the stationary problem is then

$$\left\{\begin{array}{l}\displaystyle\int_{K_i}\frac{1}{\widehat{\rho_0}}\,\varphi\mathrm{div}_{\mathbf{x}}\widehat{\mathbf{u}}+\sum_{j\in\mathcal{N}(i)}\int_{\Gamma_{ij}}\frac{\varphi}{2}\left(\frac{1}{\widehat{\rho_0}}[\![\,\widehat{\mathbf{u}}\cdot\mathbf{n}_{ij}\,]\!]-\widehat{c_0}[\![\,\widehat{p}\,]\!]\right)=0,\\ \displaystyle\int_{K_i}\widehat{\kappa_0}\boldsymbol{\psi}\cdot\nabla\widehat{p}+\sum_{j\in\mathcal{N}(i)}\int_{\Gamma_{ij}}\frac{\boldsymbol{\psi}}{2}\cdot(\widehat{\kappa_0}[\![\,\widehat{p}\mathbf{n}_{ij}\,]\!]-\widehat{c_0}[\![\,\widehat{\mathbf{u}}\cdot\mathbf{n}_{ij}\,]\!]\mathbf{n}_{ij})=0,\end{array}\right. \tag{4.4}$$

that can be rephrased as

$$\left\{\begin{array}{l}\displaystyle\int_{K_i}\frac{1}{\widehat{\rho_0}}\,\varphi\mathrm{div}_{\mathbf{x}}\widehat{\mathbf{u}}+\sum_{j\in\mathcal{N}(i)}\int_{\Gamma_{ij}}\frac{\mathrm{Tr}(\varphi)}{2}\left(\frac{1}{\widehat{\rho_0}}[\![\,\widehat{\mathbf{u}}\cdot\mathbf{n}_{ij}\,]\!]-\widehat{c_0}[\![\,\widehat{p}\,]\!]\right)=0,\\ \displaystyle\int_{K_i}\widehat{\kappa_0}\boldsymbol{\psi}\cdot\nabla\widehat{p}+\sum_{j\in\mathcal{N}(i)}\int_{\Gamma_{ij}}\frac{\mathbf{Tr}(\boldsymbol{\psi})}{2}(\widehat{\kappa_0}[\![\,\widehat{p}\,]\!]-\widehat{c_0}[\![\,\widehat{\mathbf{u}}\cdot\mathbf{n}_{ij}\,]\!])=0.\end{array}\right. \tag{4.5}$$

We aim at proving that $\frac{1}{\widehat{\rho_0}}[\![\,\widehat{p}\,]\!]-\widehat{c_0}[\![\,\widehat{\mathbf{u}}\cdot\mathbf{n}_{ij}\,]\!]=0$, and that on each cell, $\mathrm{div}_{\mathbf{x}}\widehat{\mathbf{u}}=0$ and $\nabla_{\mathbf{x}}\widehat{p}=0$. Then, (4.5) gives

$$\forall\varphi\in\mathrm{div}_{\mathbf{x}}^{\perp}\quad\forall\boldsymbol{\psi}\in\nabla_{\mathbf{x}}^{\perp}\qquad\left\{\begin{array}{l}\displaystyle\sum_{j\in\mathcal{N}(i)}\int_{\Gamma_{ij}}\frac{\mathrm{Tr}(\varphi)}{2}\left(\frac{1}{\widehat{\rho_0}}[\![\,\widehat{\mathbf{u}}\cdot\mathbf{n}_{ij}\,]\!]-\widehat{c_0}[\![\,\widehat{p}\,]\!]\right)=0,\\ \displaystyle\sum_{j\in\mathcal{N}(i)}\int_{\Gamma_{ij}}\frac{\mathbf{Tr}(\boldsymbol{\psi})}{2}(\widehat{\kappa_0}[\![\,\widehat{p}\,]\!]-\widehat{c_0}[\![\,\widehat{\mathbf{u}}\cdot\mathbf{n}_{ij}\,]\!])=0,\end{array}\right.$$

which, using $\widehat{c_0}^{\,2}=\widehat{\kappa_0}/\widehat{\rho_0}$, can be rephrased as

$$\forall\varphi\in\mathrm{div}_{\mathbf{x}}^{\perp}\quad\forall\boldsymbol{\psi}\in\nabla_{\mathbf{x}}^{\perp}\qquad\left\{\begin{array}{l}\displaystyle\sum_{j\in\mathcal{N}(i)}\int_{\Gamma_{ij}}\frac{\mathrm{Tr}(\varphi)}{2}\left(\frac{1}{\widehat{\rho_0}}[\![\,\widehat{\mathbf{u}}\cdot\mathbf{n}_{ij}\,]\!]-\widehat{c_0}[\![\,\widehat{p}\,]\!]\right)=0,\\ \displaystyle-\widehat{\rho_0}\widehat{c_0}\sum_{j\in\mathcal{N}(i)}\int_{\Gamma_{ij}}\frac{\mathbf{Tr}(\boldsymbol{\psi})}{2}\left(\frac{1}{\widehat{\rho_0}}[\![\,\widehat{\mathbf{u}}\cdot\mathbf{n}_{ij}\,]\!]-\widehat{c_0}[\![\,\widehat{p}\,]\!]\right)=0.\end{array}\right. \tag{4.6}$$

Using the result of Proposition 5 that $\mathbf{Tr}\left(\nabla_{\mathbf{x}}^{\perp}\right)+\mathrm{Tr}\left(\mathrm{div}_{\mathbf{x}}^{\perp}\right)=R_k(\partial K)$ leads to

$$\forall\hat{\phi}\in R_k(\partial K)\qquad\int_{\partial K}\hat{\phi}\left(\frac{1}{\widehat{\rho_0}}[\![\,\widehat{\mathbf{u}}\cdot\mathbf{n}_{ij}\,]\!]-\widehat{c_0}[\![\,\widehat{p}\,]\!]\right)=0,$$

so that $\frac{1}{\widehat{\rho}_0}[\![\,\widehat{\mathbf{u}}\cdot\mathbf{n}_{ij}\,]\!]-\widehat{c_0}[\![\,\widehat{p}\,]\!]=0$ is ensured. Exchanging cells i and j gives $\frac{1}{\widehat{\rho}_0}[\![\widehat{\mathbf{u}}_h\cdot\mathbf{n}_{ji}]\!]+\frac{\widehat{c_0}}{2}[\![\widehat{p}_h]\!]=0$, so that $[\![\widehat{p}_h]\!]=0$ and $[\![\widehat{\mathbf{u}}_h\cdot\mathbf{n}_{ij}]\!]=0$. As these jumps vanish, (4.4) gives

$$\begin{aligned}&\forall\boldsymbol{\psi}\in BDM_k(K_i), && \int_{K_i}\boldsymbol{\psi}\cdot\nabla_{\tilde{\mathbf{x}}}\widehat{p}_h=0,\\ &\forall\varphi\in\mathbb{P}_k(K_i), && \int_{K_i}\varphi\mathrm{div}_{\mathbf{x}}\widehat{\mathbf{u}}_h=0,\end{aligned}$$

which ends the proof.

5. Numerical results. We aim at illustrating Proposition 3 and Corollary 4.3. These two results rely on the discrete gradient $\nabla^{\mathcal{M}_h}$ and the discrete divergence $\mathrm{div}_{\mathbf{x}}^{\mathcal{M}_h}$. These two quantities are respectively in $\left(L^2(\mathcal{C})\right)^d\times\left(L^2(\mathcal{S})\right)^d$ and $L^2(\mathcal{C})\times L^2(\mathcal{S})$, and for numerically monitoring these quantities, we will use the natural Cartesian L^2 norm on this space. We therefore define on V_h and $\mathcal{V}_h$ the following seminorms:

$$\left\|\nabla^{\mathcal{M}_h}\widehat{p}_h\right\|_{\mathrm{DG}}^2=\sum_{K\in\mathcal{C}}\int_K\|\nabla\widehat{p}_h\|_2^2+\sum_{S\in\mathcal{S}}\int_S[\![\,\widehat{p}_h\,]\!]^2, \tag{5.1}$$

$$\left\|\mathrm{div}_{\mathbf{x}}^{\mathcal{M}_h}\widehat{\mathbf{u}}_h\right\|_{\mathrm{DG}}^2=\sum_{K\in\mathcal{C}}\int_K\left(\mathrm{div}_{\mathbf{x}}\widehat{\mathbf{u}}_h\right)^2+\sum_{S\in\mathcal{S}}\int_S[\![\,\widehat{\mathbf{u}}_h\cdot\mathbf{n}_S\,]\!]^2. \tag{5.2}$$

Since we focus on the low Mach number accuracy problem and since this problem does not depend on time integration, the time integration is performed in (3.5) and (3.2) using an explicit Strong Stability Preserving [19] method with a CFL number of 0.19. Similar results can be obtained using implicit time integration. For evaluating the volume and face integrals, Gauss quadrature formula are used. The number of quadrature points is chosen to integrate exactly on the reference element polynomials of degree $2k$ on cells and $2k+1$ on faces.

This section is divided into two subsections. In the first one, only the results of Proposition 3 are tested, namely we address the problem of the high order accuracy of the long time solution of the wave system. This allows us to do a first selection on the scheme for the Euler system which may be accurate or not at low Mach number. This is addressed in the second subsection. The link between the long time limit of the wave system and the low Mach number accuracy for the Euler system was extensively discussed in [25].

5.1. Wave system. In this section, we address the convergence of the long time limit of the discontinuous Galerkin method toward the long time limit of the continuous system. Existence of this limit was discussed in [24] for the finite volume case but is not clear in general. This is why we will first test whether the discrete solution is converging toward a limit at infinity.

At the continuous level, we know that the long time limit of the wave system (2.8) with boundary conditions given by (2.9) and initial condition $(\widehat{p}_0,\widehat{\mathbf{u}}_0)$ exists and is given by (2.11). From a numerical point of view, the pressure is uniform provided $\nabla^{\mathcal{M}_h}\widehat{p}_h=0$. The velocity is divergence free provided $\mathrm{div}_{\mathbf{x}}^{\mathcal{M}_h}\widehat{\mathbf{u}}_h=0$, but this is only a necessary condition, not a sufficient one, because $\mathrm{div}_{\mathbf{x}}^{\mathcal{M}_h}\widehat{\mathbf{u}}_h=0$ does not give any hint on the closeness with the exact long time velocity $\mathbf{u}_{\boldsymbol{\Psi}}(\widehat{\mathbf{u}}_0)$. As a consequence, the following properties will be tested:

- Is the numerical solution converging toward a steady state?
- If this steady state exists, which we denote by $(\widehat{p}_h,\widehat{\mathbf{u}}_h)$, then do we have $\nabla^{\mathcal{M}_h}\widehat{p}_h=0$ and $\mathrm{div}_{\mathbf{x}}^{\mathcal{M}_h}\widehat{\mathbf{u}}_h=0$?
- If $\nabla^{\mathcal{M}_h}\widehat{p}_h=0$ and $\mathrm{div}_{\mathbf{x}}^{\mathcal{M}_h}\widehat{\mathbf{u}}_h=0$, then is $\widehat{\mathbf{u}}_h$ converging toward the exact long time limit $\mathbf{u}_{\boldsymbol{\Psi}}(\widehat{\mathbf{u}}_0)$, and what is its order of convergence?

5.1.1. Vortex. The numerical dissipation of a stationary vortex is studied. The domain is the square $[0,100]\times[0,100]$ and the initial condition is given by

$$\left\{\begin{array}{l}\widehat{p}_0(x,y)=0,\\ \widehat{\mathbf{u}}_0(x,y)=\left(\begin{array}{l}-\dfrac{y-y_{\mathrm{center}}}{R}\exp\left(-\dfrac{(x-x_{\mathrm{center}})^2+(y-y_{\mathrm{center}})^2}{2\times R^2}\right)\\ \dfrac{x-x_{\mathrm{center}}}{R}\exp\left(-\dfrac{(x-x_{\mathrm{center}})^2+(y-y_{\mathrm{center}})^2}{2\times R^2}\right)\end{array}\right)\end{array}\right. \tag{5.3}$$

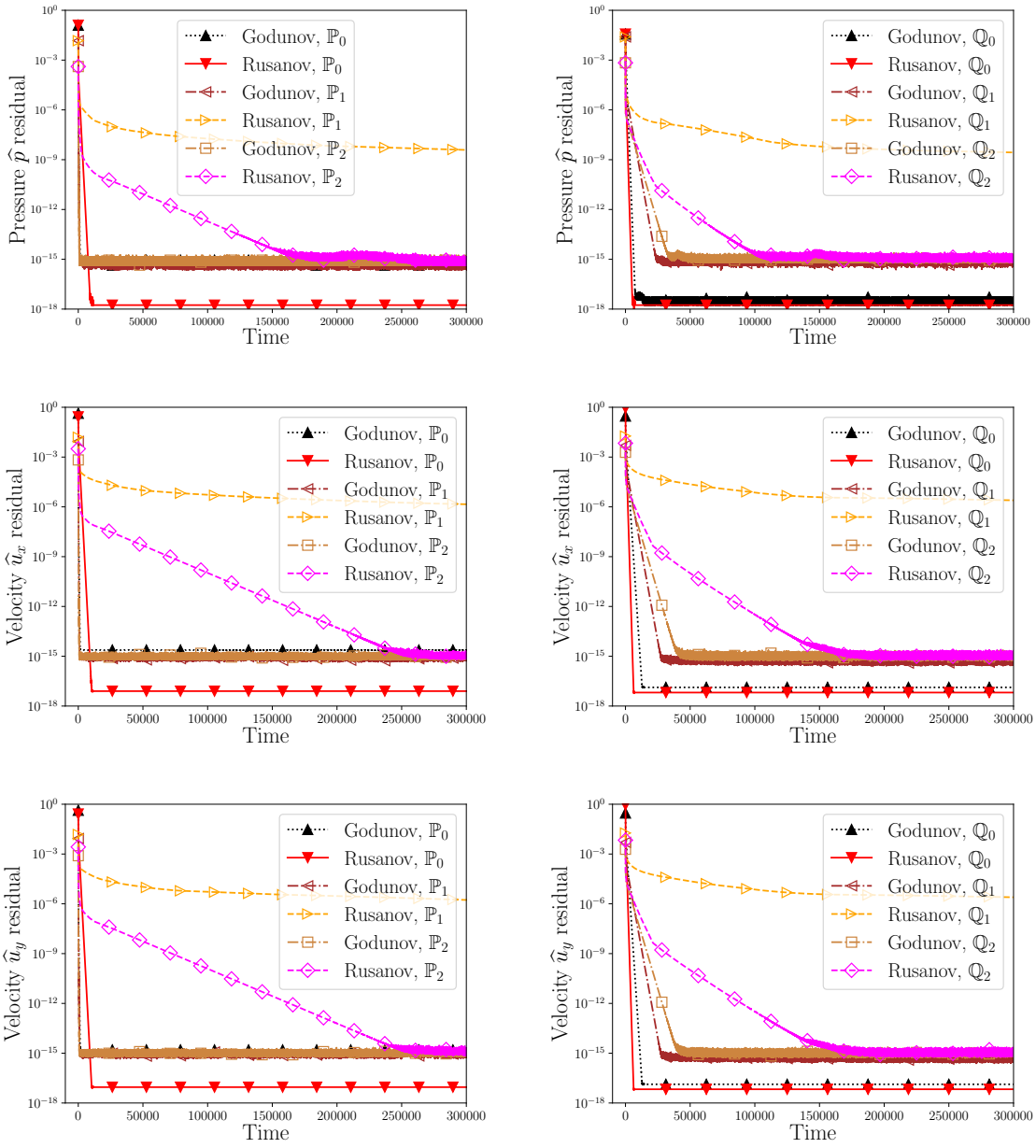

FIGURE 5.1. *Wave vortex — residuals as a function of the computational time obtained on triangular (left) and quadrangular (right) mesh for different degrees of approximation with Godunov (3.7) and Rusanov (3.8) stabilization.*

with $R = 15$ and $(x_{\text{center}}, y_{\text{center}}) = (50, 50)$. Inlet/outlet boundary conditions (2.9c) are used with $\widehat{p}_b = 0$ and $\widehat{\mathbf{u}}_b = \widehat{\mathbf{u}}_0$. Since the initial condition satisfies $\text{div}_{\mathbf{x}}(\widehat{\mathbf{u}}_0) = 0$ and the boundary condition satisfies $\widehat{\mathbf{u}}_0 \cdot \mathbf{n} = \widehat{\mathbf{u}}_b \cdot \mathbf{n}$, we have $\mathbf{u}_{\boldsymbol{\Psi}}(\widehat{\mathbf{u}}_0) = \widehat{\mathbf{u}}_0$ and $\widehat{\mathbf{u}}_0$ is a steady solution of the continuous system (2.8) with boundary condition (2.9c). Then, the exact long time limit is $(\widehat{p}_{\text{ex}}, \widehat{\mathbf{u}}_{\text{ex}}) = (0, \widehat{\mathbf{u}}_0)$.

Behavior when the time goes to infinity. In Figure 5.1, the pressure residual and the velocities residuals are plotted as a function of the time. A triangular mesh containing 540 cells and a Cartesian mesh containing 256 cells are used. Even if the time required depends on the stabilization and the degree of approximation used, all these schemes (except the Rusanov scheme with a degree of approximation equals to one) allow a steady state to be reached.

About $\|\nabla \widehat{p}_h\|_{DG}$ and $\|\text{div}_{\mathbf{x}} \widehat{\mathbf{u}}_h\|_{DG}$ of the long time limit. We now study if the long time limit of the wave system ensures a null pressure field and a divergence free velocity field. In Figure 5.2, the seminorms $\|\nabla \widehat{p}_h\|_{\text{DG}}$ and $\|\text{div}_{\mathbf{x}} \widehat{\mathbf{u}}_h\|_{\text{DG}}$ defined by (5.1) and (5.2) of the long time limit of the wave

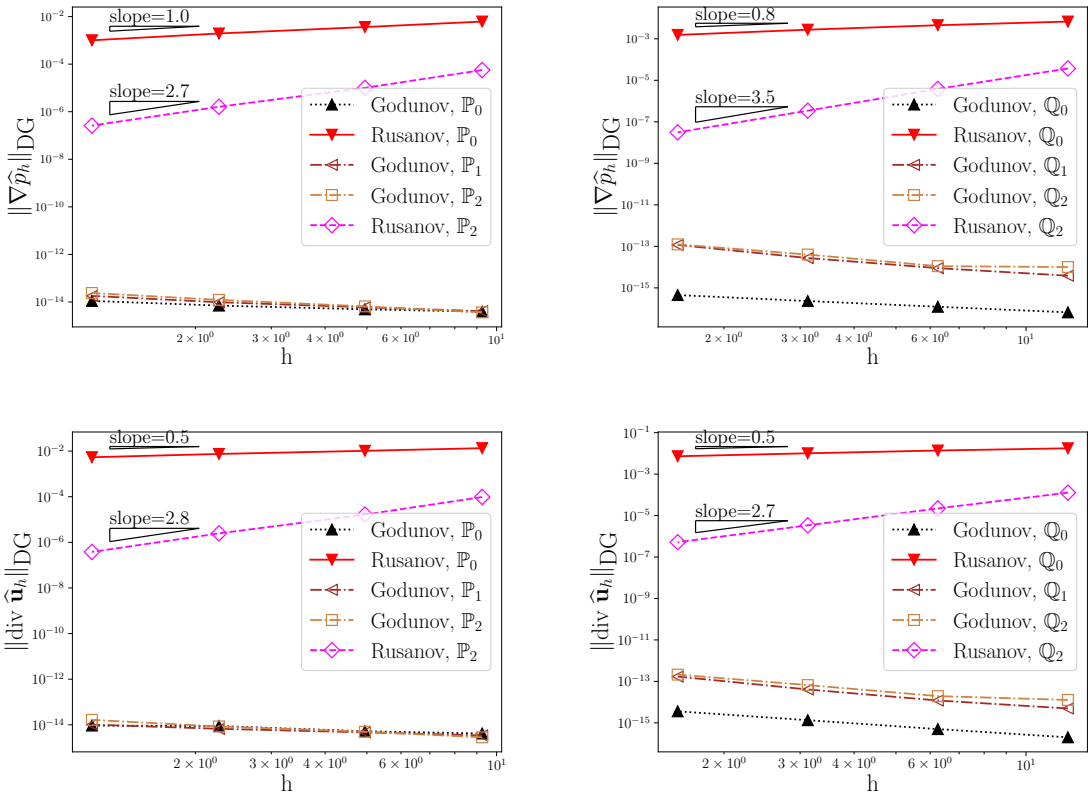

FIGURE 5.2. *Wave vortex — norms* $\|\nabla \widehat{p}_h\|_{DG}$ *and* $\|\mathrm{div}_{\mathbf{x}} \widehat{\mathbf{u}}_h\|_{DG}$ *defined by* (5.1) *and* (5.2) *of the long time numerical solution obtained for different degrees of approximation on triangular meshes (left) and Cartesian meshes (right) with Godunov* (3.7) *and Rusanov* (3.8) *stabilizations. A log-log plot is used.*

system for different triangular and Cartesian meshes are plotted. Four different triangular meshes are used containing respectively 116, 540, 2 250 and 9 248 cells. Cartesian meshes contain respectively 64, 256, 1 024 and 4 096 cells. Since the Rusanov scheme with a degree of approximation equal to one does not converge to a steady state, these results are not plotted in Figure 5.2. The results on triangular meshes are in agreement with Proposition 3. With the Godunov scheme, the long time limit has a uniform pressure and a divergence free velocity field. This property seems also to be satisfied for the Godunov scheme on Cartesian meshes. Using the Rusanov scheme, the long time pressure limit is not uniform and the long time velocity is not divergence free.

Convergence study of the long time limit. Results of Figure 5.2 show that using the Godunov scheme, the long time velocity field is divergence free. This condition is necessary but not sufficient to approximate accurately the long time limit of the continuous system. Indeed, the long time solution of the numerical scheme may be constant and so divergence free whereas the exact solution may not be constant. To study if the long time solution approximates correctly the exact solution, a mesh convergence study is performed in Figure 5.3. With the Godunov scheme on triangular meshes, the long time pressure is uniform and equal to zero and the velocity is converging toward the exact solution with a rate of $k+1$ for $\mathbb{P}_k$ finite elements. On Cartesian meshes or with the Rusanov scheme on triangular meshes, the velocity does not converge toward the exact solution with the optimal convergence rate. Indeed, a rate of k (instead of $k+1$) for $\mathbb{Q}_k$ or $\mathbb{P}_k$ finite elements is observed.

Conclusion. From the results of Figures 5.1, 5.2, and 5.3, we remark that as for finite volume method [22, 20, 34, 32, 13], the discontinuous Galerkin scheme with

- a Rusanov stabilization (3.8) does not give a long time limit that is optimal order, neither with triangular mesh nor with Cartesian mesh;
- a Godunov stabilization (3.7) has different behavior depending on the mesh geometry. The long time limit has an optimal order of convergence on triangular meshes but not on Cartesian meshes.

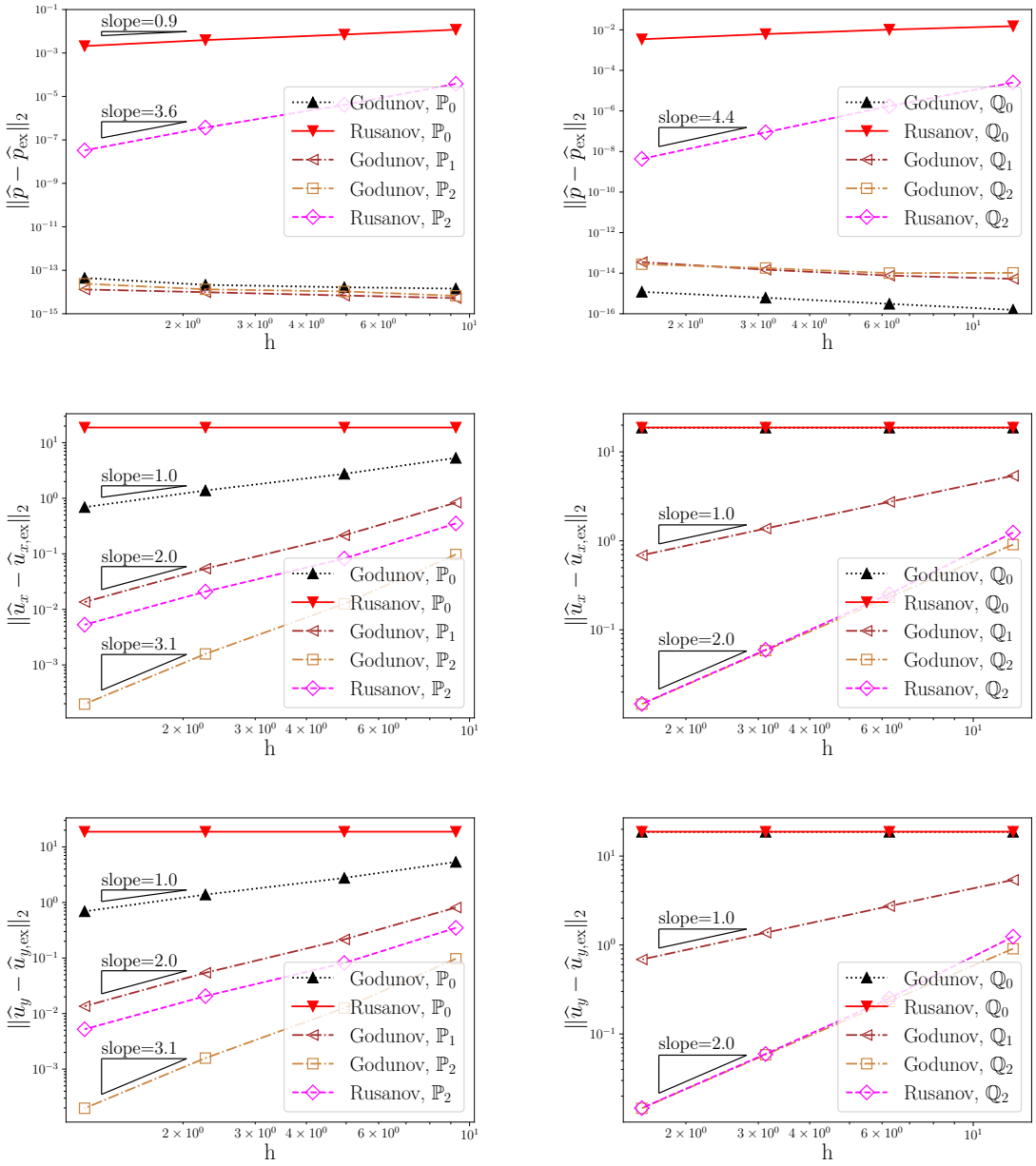

FIGURE 5.3. *Wave vortex — L^2 norm of the error between the exact solution and the long time numerical solution obtained with Godunov (3.7) and Rusanov (3.8) stabilizations and different degrees of approximation on triangular (left) and Cartesian (right) meshes. A log-log plot is used.*

5.1.2. Cylinder scattering. We want to test the Godunov scheme on a more complex geometry with an initial condition far from the exact solution. We consider the problem of the scattering of a wave by a cylinder of radius r_0. The domain Ω is an annulus $[r_0, r_1] \times [0, 2\pi[$. Here, we use $r_0 = 0.5$ and $r_1 = 5.5$. A wall boundary condition (2.9b) is used in $r = r_0$ and an inlet/outlet boundary condition (2.9c) is used in $r = r_1$ with $\widehat{p}_b = 0$ and $\widehat{\mathbf{u}}_b = (1, 0)^T$. The initial data are uniform and set equal to

$$\widehat{p}_h = 0, \qquad \widehat{\mathbf{u}}_h = 0.$$

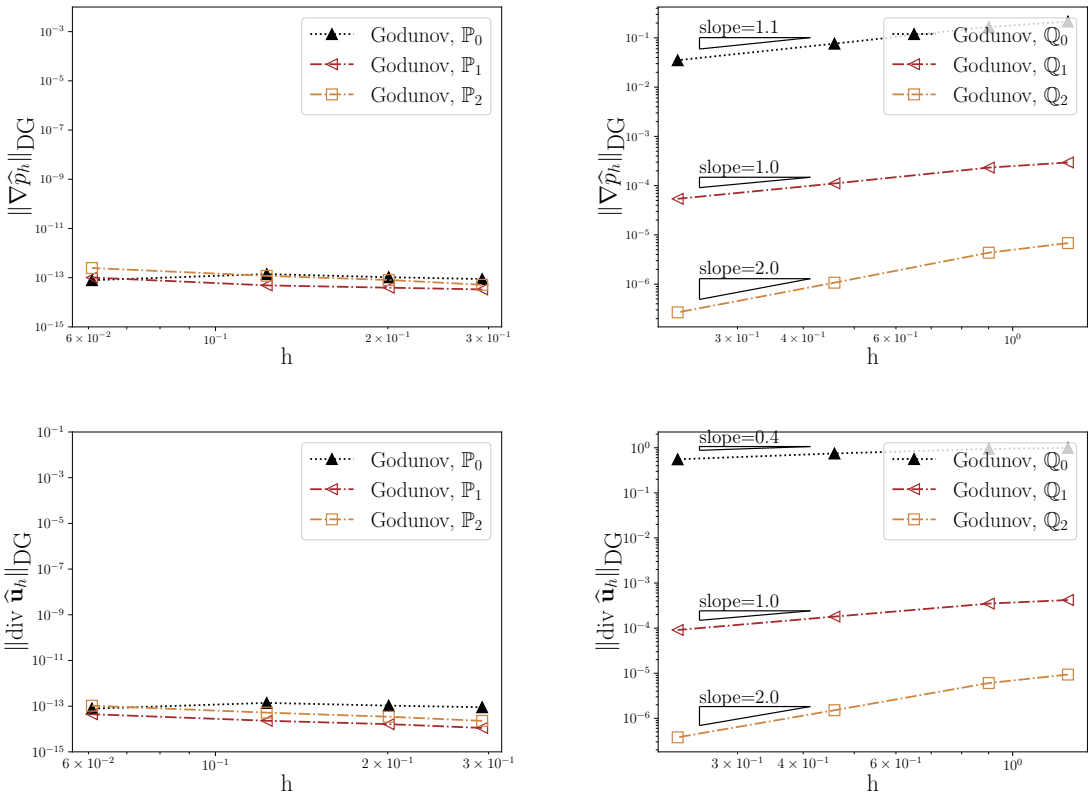

FIGURE 5.4. *Wave cylinder scattering - norms* $\|\nabla \widehat{p}_h\|_{DG}$ *and* $\|\mathrm{div}_{\mathbf{x}} \widehat{\mathbf{u}}_h\|_{DG}$ *defined by* (5.1) *and* (5.2) *of the long time numerical solution obtained for different degrees of approximation with the Godunov stabilization* (3.7) *on triangular (left) and quadrangular (right) straight meshes. A log-log plot is used.*

Then, the exact long time limit is given by

$$\left\{ \begin{array}{l} \widehat{p}_{\mathrm{ex}} = 0, \\ \\ \widehat{\mathbf{u}}_{\mathrm{ex}}(r,\theta) = \widehat{\mathbf{u}}_{\mathbf{\Psi}}(\widehat{\mathbf{u}}_0) = \dfrac{r_1^2}{r_1^2 - r_0^2} \begin{pmatrix} 1 - \dfrac{r_0^2}{r^2}\cos(2\theta) \\ -\dfrac{r_0^2}{r^2}\sin(2\theta) \end{pmatrix}. \end{array} \right. \tag{5.4}$$

About $\|\nabla \widehat{p}_h\|_{DG}$ *and* $\|\mathrm{div}_{\mathbf{x}} \widehat{\mathbf{u}}_h\|_{DG}$ *of the long time limit.* We first study if the long time limit of the wave system obtained with the Godunov scheme on a more complex geometry has a uniform pressure and a divergence free velocity field. In Figure 5.4, the seminorms $\|\nabla \widehat{p}_h\|_{\mathrm{DG}}$ and $\|\mathrm{div}_{\mathbf{x}} \widehat{\mathbf{u}}_h\|_{\mathrm{DG}}$ of the long time limit are plotted for different straight triangular and quadrangular meshes. Four different triangular meshes are used containing respectively 1 598, 3 430, 9 184 and 35 988 cells. The quadrangular meshes are structured and contain respectively 72, 200, 800 and 3 200 cells. They are obtained using a resolution of n_r in the radial direction and n_θ in the orthoradial direction with respectively $(n_r, n_\theta) = (6, 12)$, $(n_r, n_\theta) = (10, 20)$, $(n_r, n_\theta) = (20, 40)$, and $(n_r, n_\theta) = (40, 80)$. With the Godunov scheme on triangular meshes, as expected, the long time limit has a uniform pressure and a divergence free field. On quadrangular meshes, the long time limit does not have a uniform pressure nor a divergence free velocity field.

Convergence study of the long time limit. In Figure 5.5, a mesh convergence study is performed, in which the error between the exact solution (5.4) and the long time limit of the discrete solution is computed. Since the boundaries of the domain are curved, the optimal order can be reached only if the mesh is curved too [4]. However, some difficulties to reach a long time limit with the Godunov scheme and curved meshes were observed. We also note that we were not able to reach a steady state using curved quadrangular meshes. Note, however, that

- the theoretical result Proposition 3 was proven only on straight meshes, so that the difficulties encountered in the curved mesh case do not contradict this result,

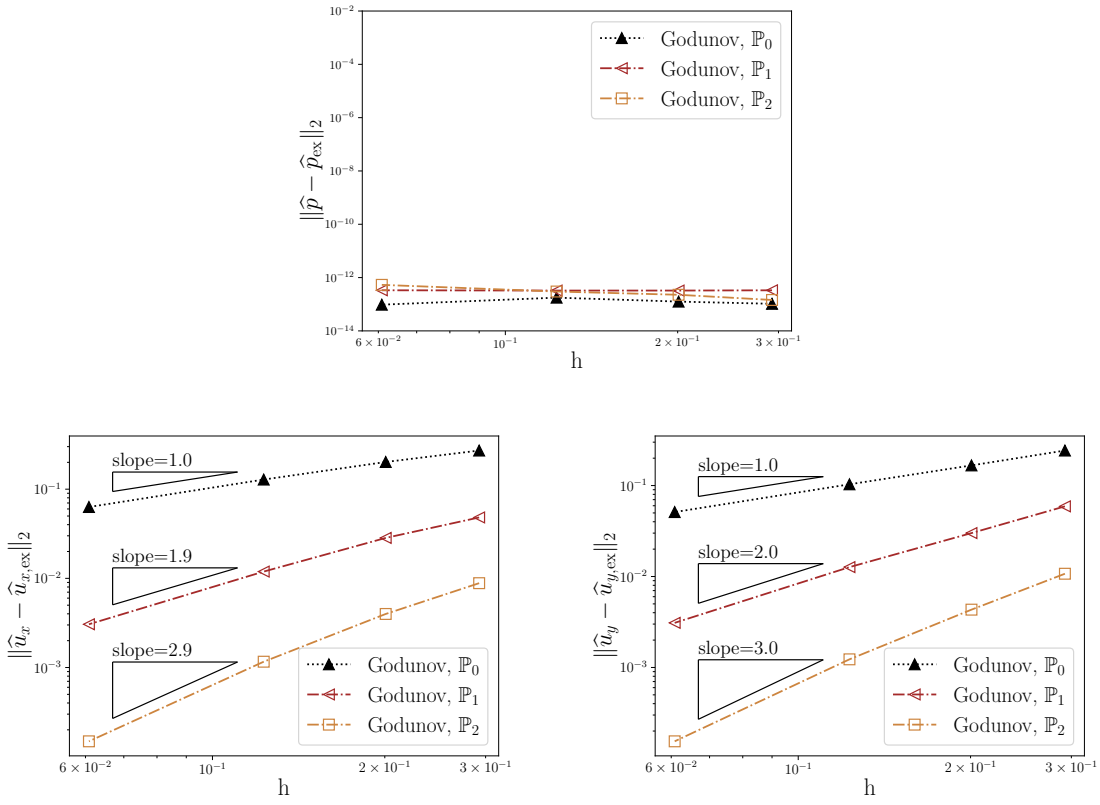

FIGURE 5.5. *Wave cylinder scattering — L^2 norm of the error between the exact solution and the numerical solution obtained with $\mathbb{P}_0$, $\mathbb{P}_1$, and $\mathbb{P}_2$ finite elements with the Godunov scheme (3.7) and a slip wall boundary condition (5.5) on the cylinder. A log-log plot is used.*

- the quadrangular meshes case and the Rusanov scheme with the triangular meshes were already proven to fail in the previous test case, so the only thing we are interested in here is whether the triangular case with the Godunov scheme is optimal order or not.

To remove difficulties, a curved mesh was kept only for the cylinder (in $r = r_0$). A straight approximation of the circle $r = r_1$ and a Steger–Warming boundary condition where the exact solution is weakly imposed was used for all the following simulations.

The meshes are the same meshes as in Figure 5.4 with a second order approximation of the cylinder in $r = r_0$. To improve the convergence toward a steady state, the classical wall boundary condition (2.9b) is replaced by a slip wall boundary condition [3]

$$\begin{bmatrix} \frac{1}{\widehat{\rho}_0}\widehat{\mathbf{u}}\cdot\mathbf{n} \\ \widehat{\kappa_0}\widehat{p}\mathbf{n} \end{bmatrix}_{\text{slipWall}} = \begin{pmatrix} 0 \\ \widehat{\kappa_0}\widehat{p}\mathbf{n} \end{pmatrix}. \tag{5.5}$$

We observe in Figure 5.5 that the long time limit ensures a null pressure field. Also, velocity is converging toward the exact solution with the optimal rate of $k+1$ for $\mathbb{P}_k$ finite elements.

Conclusion. From Figures 5.4 and 5.5, we confirm that the discontinuous Galerkin method with a Godunov flux does not have a long time limit convergence with optimal order on quadrangular meshes but it does on triangular meshes. With quadrangular meshes, instead of Cartesian ones, the long time limit obtained with the Godunov flux has no more a uniform pressure field nor a divergence free velocity field. Last, the optimal mesh convergence rate is obtained with the Godunov flux on curved triangular meshes.

5.2. Euler equation. We aim at illustrating the low Mach number accuracy of the discontinuous Galerkin method with a Roe numerical flux on triangular meshes. For all the following simulations, we consider the barotropic Euler equation (2.1) using the pressure law $p(\rho) = \kappa\rho^\gamma$ where $\kappa = 1$ and $\gamma = 2$.

5.2.1. Vortex. This test case is the nonlinear version of the test case performed in subsubsection 5.1.1. The isentropic vortex is defined by its density ρ_∞ and Mach number M_∞ at infinity. The initial condition is given by

$$\begin{cases} \mathbf{u}_0(\mathbf{x}) = u_\infty \hat{\mathbf{u}}_0, \\ \rho_0(\mathbf{x}) = \rho_\infty - \dfrac{1}{2}\rho_\infty \exp\left(-\dfrac{(x - x_{\text{center}})^2 + (y - y_{\text{center}})^2}{2 \times R^2}\right) M_\infty^2, \end{cases}$$

where $u_\infty = M_\infty \sqrt{p'(\rho_\infty)}$ and $\hat{\mathbf{u}}_0$ is given by (5.3). The initial condition matches with the exact incompressible solution $(\rho_{\text{ex}}^{\text{Incomp}}, \mathbf{u}_{\text{ex}}^{\text{Incomp}})$ which is a stationary solution of the incompressible system. The exact solution is weakly imposed at all the boundaries with the Steger–Warming boundary condition (2.2b). For the numerical test, $\rho_\infty = 2$ was used. The same meshes and parameters are used as in subsubsection 5.1.1. For balancing the effect of the order of accuracy, the final computational time is increased when the order of accuracy is increased: the final time is $t = 100$ s for $\mathbb{P}_0$, $t = 30\,000$ s for $\mathbb{P}_1$ and $t = 100\,000$ s for $\mathbb{P}_2$.

Iso-contours of the solution. In Figure 5.6, the iso-contours of the velocity field at final time for $M_\infty = 10^{-5}$ are plotted. In agreement with the linear case, all the results obtained with the Roe scheme seems to be low Mach number accurate. The results with the Rusanov scheme for $\mathbb{P}_0$ and $\mathbb{P}_1$ are clearly more dissipated than the results with the Roe scheme. Surprisingly, the result obtained with the $\mathbb{P}_2$ finite element and with the Rusanov scheme looks pretty fair. For performing a more thorough study, a study of the density fluctuations is performed within a mesh convergence study.

Behavior of $\|\nabla\tilde{\rho}_h\|_{\text{DG}}$ and $\|\text{div}_{\mathbf{x}}(\tilde{\rho}\tilde{\mathbf{u}})\|_{\text{DG}}$ with respect to the time. In Figure 5.7, the norms $\|\nabla\tilde{\rho}_h\|_{\text{DG}}$ and $\|\text{div}_{\mathbf{x}}(\tilde{\rho}\tilde{\mathbf{u}})\|_{\text{DG}}$ are plotted with respect to the time iteration for a Mach number $M_\infty = 10^{-5}$. In contrast to Rusanov's flux, Roe's flux converges much faster to a discrete steady solution. Moreover, a strong disparity is observed in the order of magnitude of the gradient $\|\nabla\tilde{\rho}_h\|_{\text{DG}}$ and the divergence $\|\text{div}_{\mathbf{x}}(\tilde{\rho}\tilde{\mathbf{u}})\|_{\text{DG}}$ between the two numerical methods.

Behavior of $\|\nabla\tilde{\rho}_h\|_{\text{DG}}$ and $\|\text{div}_{\mathbf{x}}(\tilde{\rho}\tilde{\mathbf{u}})\|_{\text{DG}}$ when $M_\infty \to 0$. In Figure 5.8, the norms $\|\nabla\tilde{\rho}_h\|_{\text{DG}}$ and $\|\text{div}_{\mathbf{x}}(\tilde{\rho}\tilde{\mathbf{u}})\|_{\text{DG}}$ are plotted with respect to the Mach number for $M_\infty = 10^{-2}$ to $M_\infty = 10^{-6}$. The results are in agreement with the results of Theorem 4.3. As expected, an $\mathcal{O}\left(M^2\right)$ scaling of the density gradient and an $\mathcal{O}\left(M\right)$ scaling of the divergence of the velocity are obtained with the Roe numerical flux.

These results are compared with the ones obtained with the Rusanov numerical flux. With the Rusanov numerical flux and $\mathbb{P}_0$ and $\mathbb{P}_1$ finite elements, an $\mathcal{O}\left(M\right)$ scaling of the density gradient and an $\mathcal{O}\left(1\right)$ scaling of the velocity divergence are obtained.

The $\mathbb{P}_2$ case deserves more comments. It seems to be low Mach number accurate for $M_b \geqslant 10^{-4}$, but no more accurate for lower Mach number. The asymptotic expansion of the density reads

$$\tilde{\rho}_h = \tilde{\rho}^{(0)} + M\tilde{\rho}_h^{(1)} + M^2\tilde{\rho}_h^{(2)} + \mathcal{O}\left(M^3\right),$$

where $\tilde{\rho}_h^{(1)}$ is the long time limit of the wave system (see [25] for the link between the low Mach number solution and the long time limit of the wave system). It was observed in subsubsection 5.1.2 that $\tilde{\rho}_h^{(1)} \neq 0$ with the Rusanov numerical flux. When $\tilde{\rho}_h^{(1)}$ is negligible with respect to $M\tilde{\rho}_h^{(2)}$, the $\mathcal{O}\left(M^2\right)$ behavior is observed (typically when $M_b \geqslant 10^{-4}$), whereas when $M\tilde{\rho}_h^{(2)}$ is negligible with respect to $\tilde{\rho}_h^{(1)}$, the $\mathcal{O}\left(M\right)$ is observed.

In Figure 5.9, a mesh convergence study at $M_\infty = 10^{-4}$ is performed. The conclusion is the same as for the linear case: with the Roe scheme on triangles, all variables converge toward the exact solution with a rate of $k+1$ with $\mathbb{P}_k$ finite elements.

From Figures 5.6 and 5.8, we deduce that it may not be sufficient to plot iso-contours to study the low Mach number behavior of a numerical scheme. It is necessary to study the pressure fluctuation with respect to the Mach number and to perform a mesh convergence study. With the Godunov scheme on triangular mesh, the pressure fluctuations scale at order $\mathcal{O}\left(M^2\right)$ and the divergence of the velocity field scales at order $\mathcal{O}\left(M\right)$. Moreover, all variables converge to the exact incompressible solution with a convergence rate of $k+1$ with $\mathbb{P}_k$ finite elements.

5.2.2. Cylinder scattering. This test case is the nonlinear version of the test case performed in subsubsection 5.1.2. Wall boundary conditions are applied on the cylinder while Steger–Warming boundary conditions with a state characterized by its density at infinity ρ_b and its Mach number at

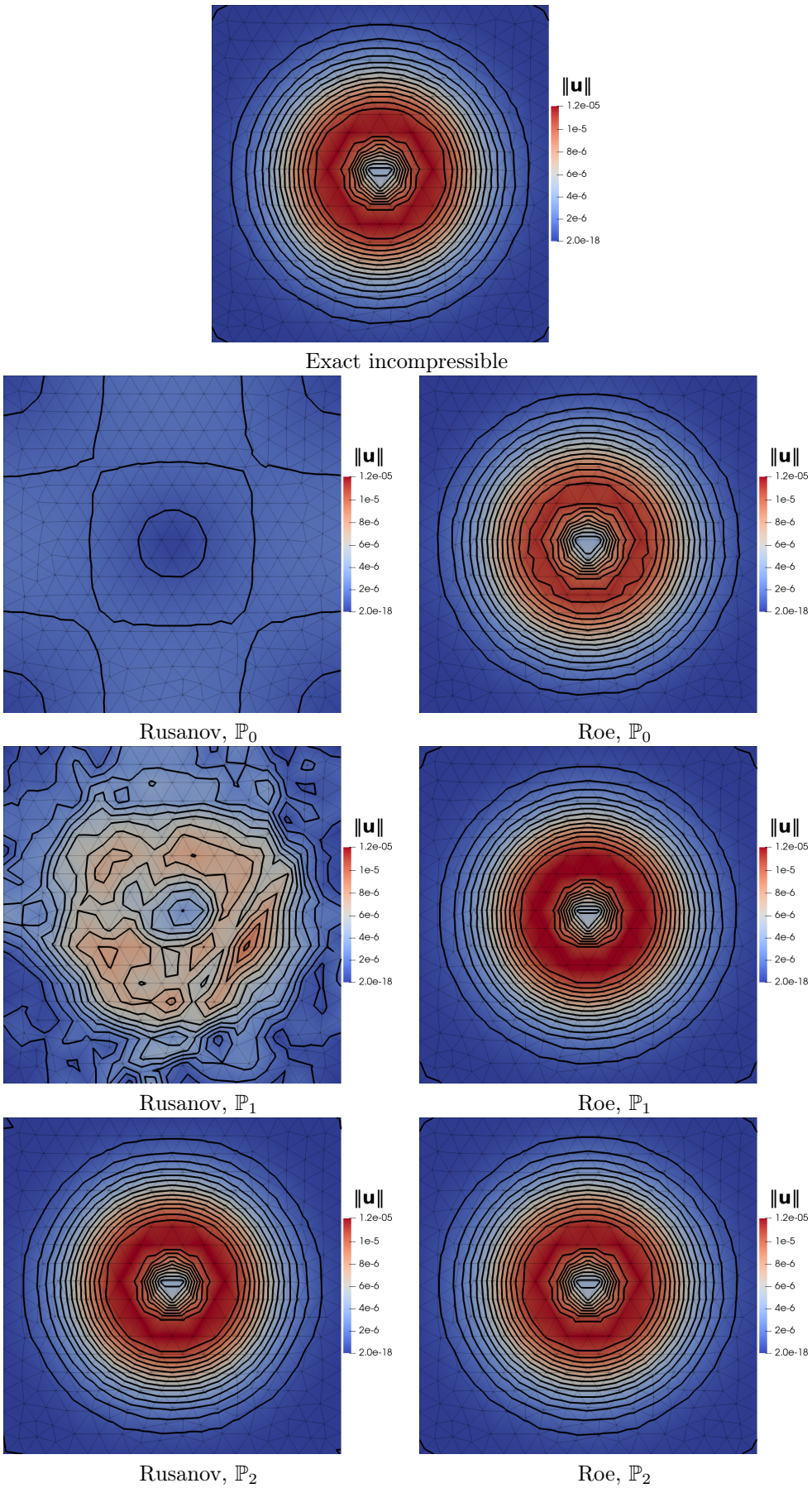

FIGURE 5.6. *Euler vortex - iso-contours of the norm of the velocity obtained at Mach number* $M_\infty = 10^{-5}$ *on triangular mesh. Fifteen equally reparted contours between* 4×10^{-9} *and* 1.1×10^{-5} *are plotted.*

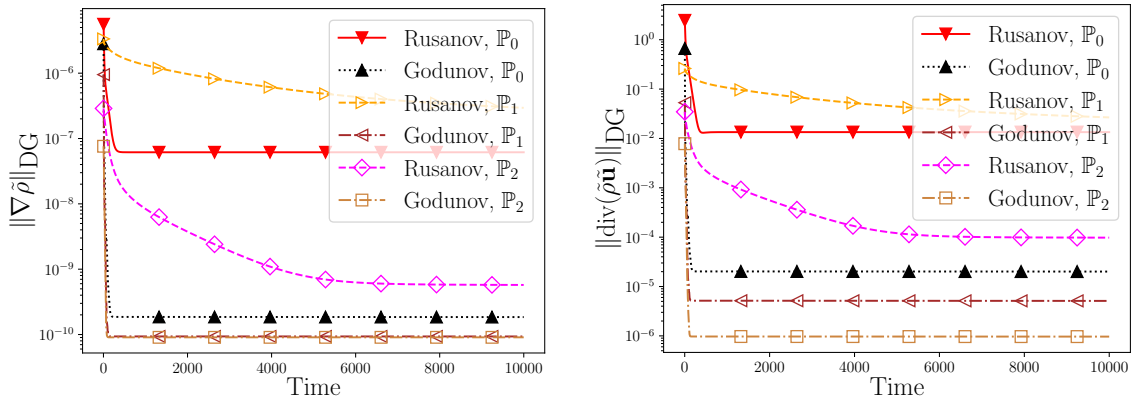

FIGURE 5.7. *Euler vortex - norms* $\|\nabla\tilde{\rho}_h\|_{\mathrm{DG}}$ *and* $\|\mathrm{div}_{\mathbf{x}}(\tilde{\rho}\tilde{\mathbf{u}})\|_{\mathrm{DG}}$ *with respect to the time for a Mach number* $M_\infty = 10^{-5}$*. Rusanov and Roe schemes are used on triangular mesh with different degree of approximation (*$\mathbb{P}_0$*,* $\mathbb{P}_1$ *and* $\mathbb{P}_2$*).*

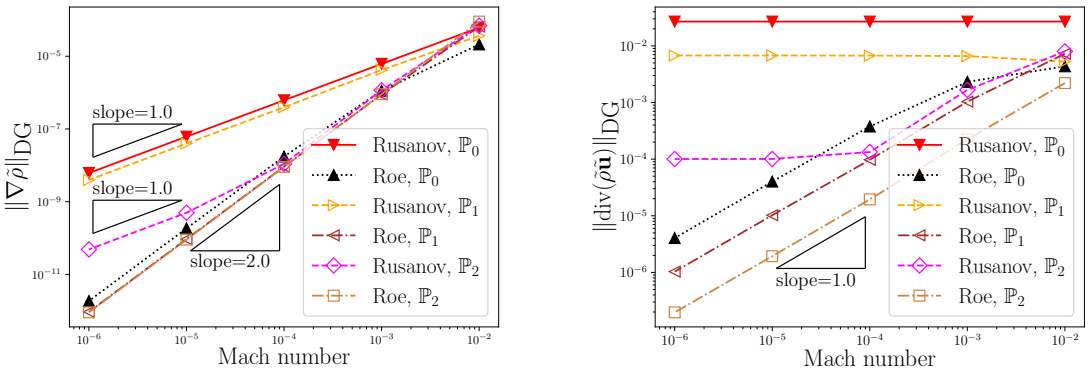

FIGURE 5.8. *Euler vortex - norms* $\|\nabla\tilde{\rho}_h\|_{\mathrm{DG}}$ *and* $\|\mathrm{div}_{\mathbf{x}}(\tilde{\rho}\tilde{\mathbf{u}})\|_{\mathrm{DG}}$ *with respect to the Mach number (for* $M_\infty = 10^{-2}$ *to* $M_\infty = 10^{-6}$*). Rusanov and Roe schemes are used on triangular mesh with different degrees of approximation (*$\mathbb{P}_0$*,* $\mathbb{P}_1$*, and* $\mathbb{P}_2$*). A log-log plot is used.*

infinity M_b. For all the computations, an external density of ρ_b is imposed, and the external velocity is deduced from the Mach number by $\mathbf{u}_b = (M_b\sqrt{p'(\rho_b)}, 0)^T$. The initial data are uniform and set equal to

$$\rho_h = \rho_b, \qquad \mathbf{u}_h = 0.$$

An approximated solution can be computed as follows: first, the velocity is harmonic and computed as in subsubsection 5.1.2. Then the pressure is computed by integrating the momentum equation, which leads to

$$\begin{cases} \mathbf{u}_{\mathrm{ex}}^{\mathrm{Incomp}}(r,\theta) = u_b\hat{\mathbf{u}}_{\mathrm{ex}}(r,\theta), \\ \rho_{\mathrm{ex}}^{\mathrm{Incomp}}(r,\theta) = \rho_b + \rho_b\left(\dfrac{r_1^2}{r_1^2 - r_0^2}\right)^2\left(\dfrac{r_0^2}{r^2}\cos(2\theta) - \dfrac{r_0^4}{2\,r^4}\right)M_b^2 \end{cases}$$

where $u_b = M_b\sqrt{p'(\rho_b)}$ and $\hat{\mathbf{u}}_{\mathrm{ex}}$ is given by (5.4). The same meshes (curved meshes in $r = r_0$) and parameters are used as in subsubsection 5.1.2. For the numerical tests, ρ_b is set to 2. From a numerical point of view, Steger–Warming boundary conditions are applied in r_1 using the exact solution at boundary and wall boundary conditions are applied in r_0 using the slip wall boundary condition of [3].

In Figure 5.10, the iso-contours of the steady velocity field are plotted for $M_b = 10^{-4}$ with a triangular mesh. The solution obtained with the Roe scheme seems to be in agreement with the exact incompressible solution. As previously explained, this study is not sufficient to conclude on the low Mach number behavior of the scheme. This is why the density fluctuations are plotted with respect to the Mach number in Figure 5.11. These fluctuations scale as $\mathcal{O}\left(M^2\right)$. Also a mesh convergence study

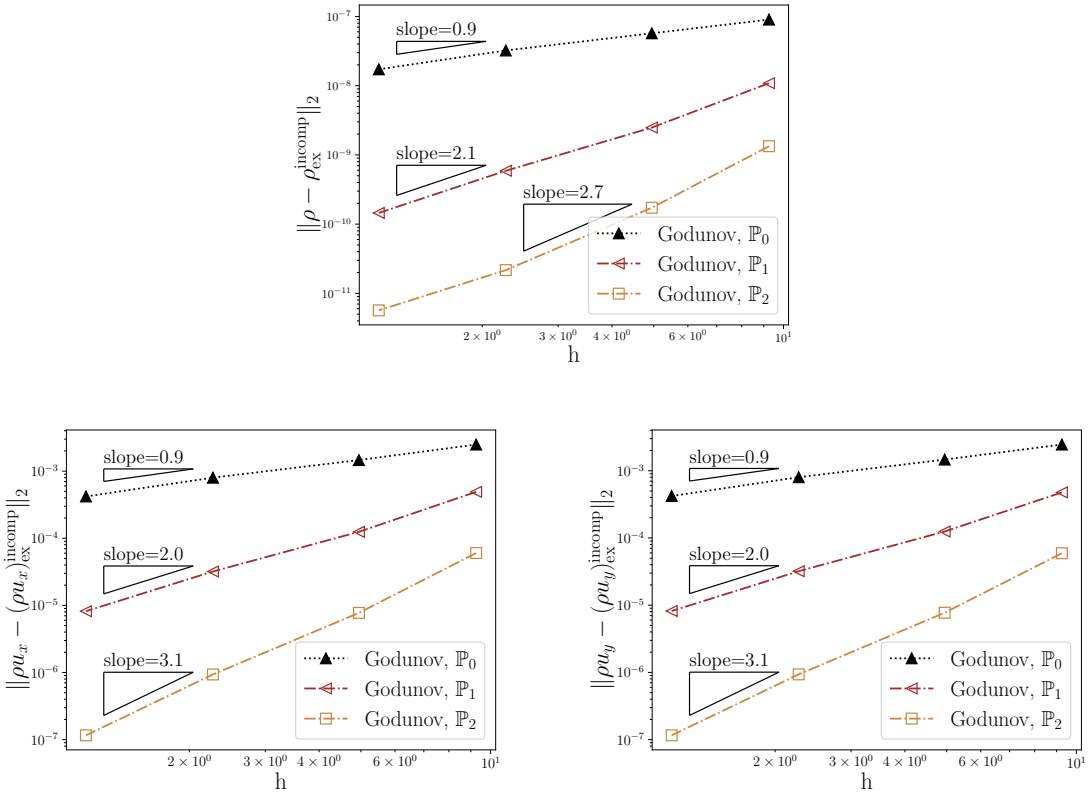

FIGURE 5.9. *Euler vortex - L^2 norm of the error between the exact incompressible solution and the numerical solution obtained with the Roe scheme and different degree of approximation. Results are shown for a Mach number of $M_\infty = 10^{-4}$. A log-log plot is used.*

at Mach number M_b equal to 10^{-4} is performed and shown in Figure 5.12. The numerical solution is converging toward the exact incompressible solution with a rate of $k + \frac{1}{2}$ for $\mathbb{P}_k$ finite elements. Thus the Roe scheme is low Mach number accurate on triangular meshes.

6. Conclusion. In this article, the behavior of the discontinuous Galerkin method for compressible flows was studied in the low Mach number limit. A result that was previously proven for finite volume schemes on triangular meshes was extended to the high order case. This result states that

- if the numerical flux preserves contacts (namely Roe, Osher, HLLC, Godunov, etc.),
- if the mesh is triangular,

then the discontinuous Galerkin method is low Mach number accurate. The numerical results state that this result is sharp, in the sense that with another type of mesh, for example, quadrangular meshes, or with a numerical flux that does not preserve contacts, the discontinuous Galerkin method is not low Mach number accurate.

The nonaccuracy in the low Mach number limit is known to give a numerical scheme that is not convergent with a finite volume scheme. The numerical results for the discontinuous Galerkin method are less disastrous: the observed order of accuracy is one order lower than the optimal order. The numerical scheme with a $\mathbb{P}_k$ or $\mathbb{Q}_k$ scheme remains convergent for $k \geqslant 1$, but with an order k.

For order 3, it was observed that the low Mach number inaccuracy may be counterbalanced by the high order nature of the numerical scheme: for moderate low Mach number ($M > 10^{-4}$), the solution looks fair, and the pressure seems to behave as $\mathcal{O}\left(M^2\right)$. Still for lower Mach number, the wrong $\mathcal{O}\left(M\right)$ behavior was observed.

Some problems were observed with classical wall boundary conditions on curved meshes, which could be solved by using slip wall boundary conditions. We have no explanation for the moment on the origin of this problem, but we will investigate this in future work.

This paper deals with isentropic Euler equations but the results can be easily extented to the full Euler system with perfect gas or stiffened gas pressure laws. Indeed, assuming that the initial condition

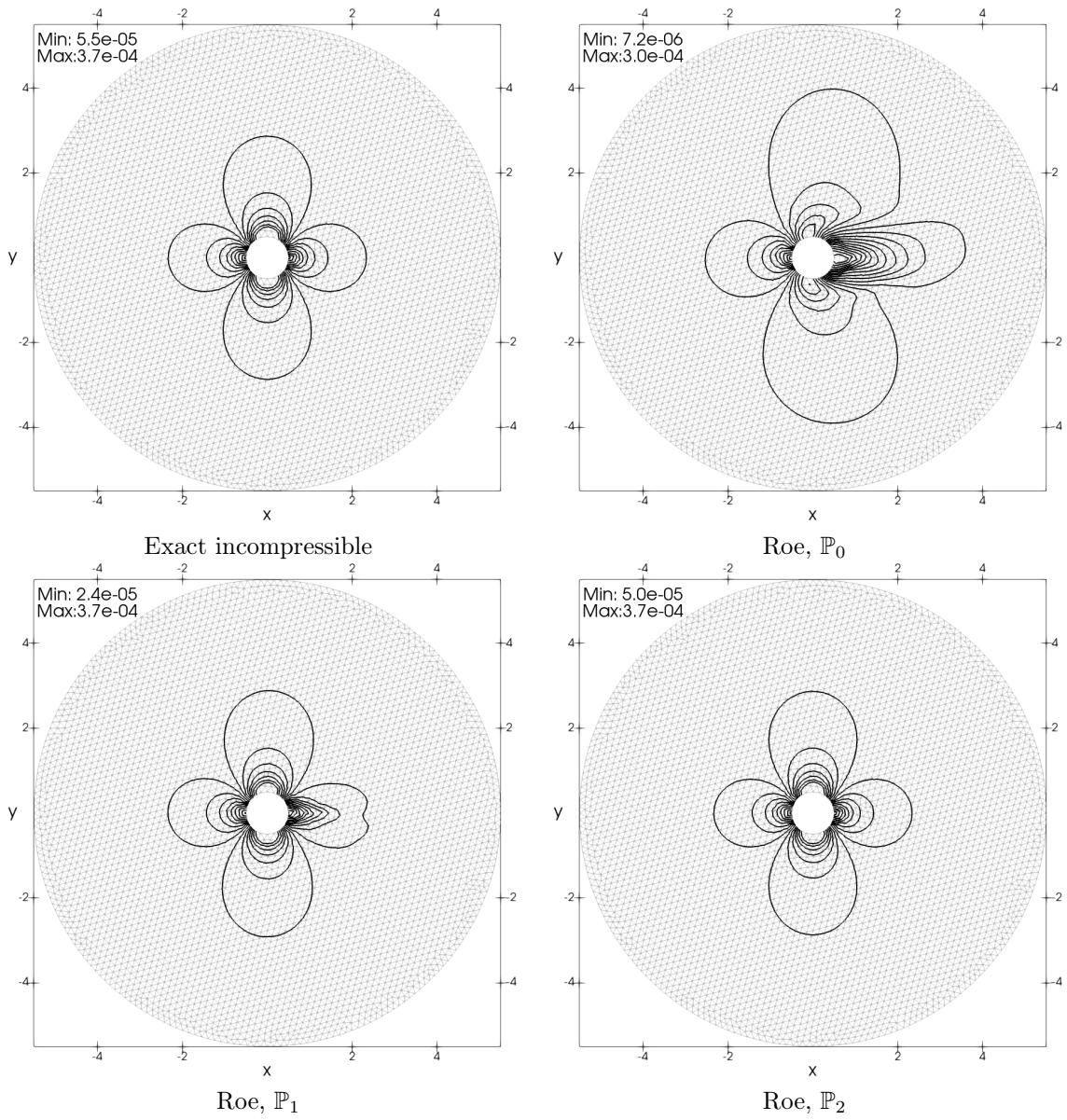

FIGURE 5.10. *Iso-contours of the norm of the velocity obtained at Mach number $M_b = 10^{-4}$ on triangular mesh. Twenty equally reparted contours between 8×10^{-6} and 3×10^{-4} are plotted.*

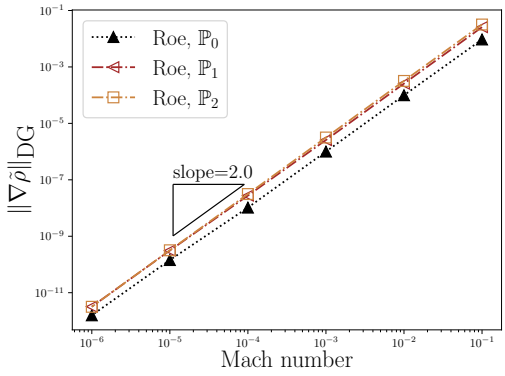

FIGURE 5.11. *Euler cylinder scattering - L^2 norm of the density fluctuation $\rho - \rho_b$ with respect to the Mach number (for $M_b = 10^{-1}$ to $M_b = 10^{-6}$). A log-log plot is used.*

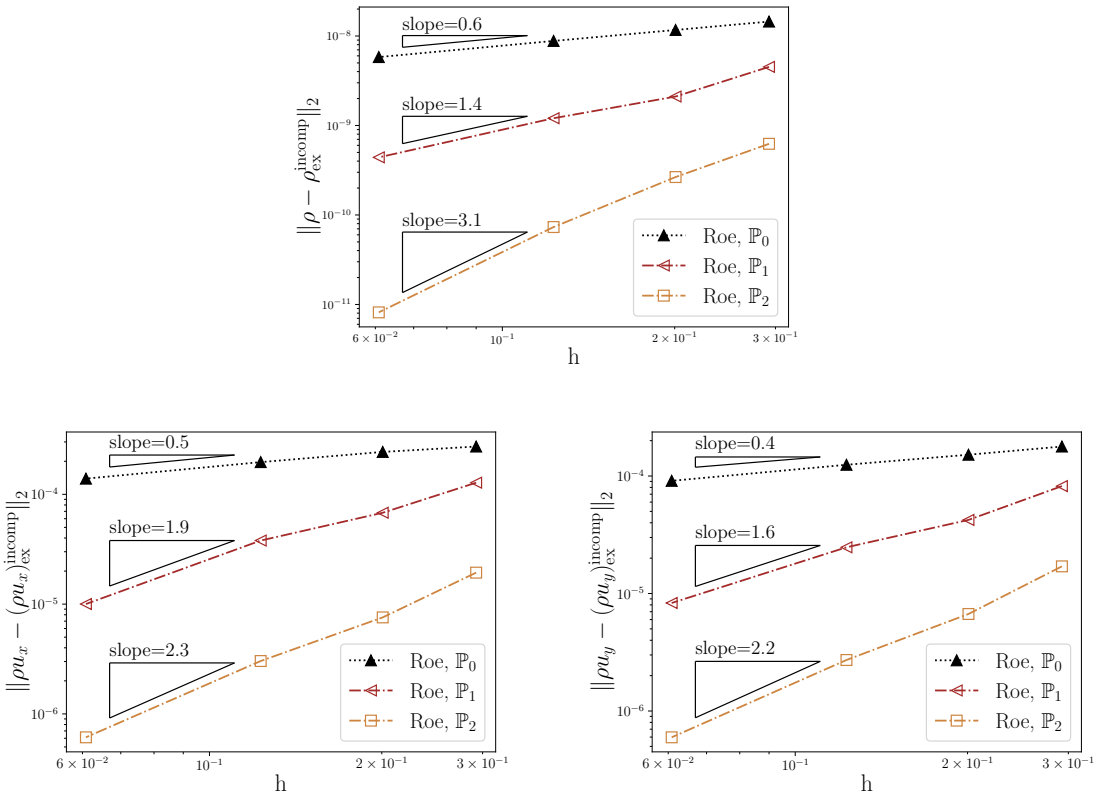

FIGURE 5.12. *Euler cylinder scattering - L^2 norm of the error between the exact incompressible solution and the numerical solution obtained with the Roe scheme and different degree of approximation. Results are shown for a Mach number of $M_b = 10^{-4}$. A log-log plot is used.*

and boundary condition are *well-prepared* in the sense that

$$\begin{cases} \tilde{\rho}(\tilde{\mathbf{x}},\tilde{t}) = \tilde{\rho}_0^{(0)} + \mathcal{O}(M), \\ \tilde{p}(\tilde{\mathbf{x}},\tilde{t}) = \tilde{p}_0^{(0)} + \mathcal{O}\left(M^2\right), \\ \tilde{\mathbf{u}}(\tilde{\mathbf{x}},\tilde{t}) = \tilde{\mathbf{u}}_0^{(0)}(\tilde{\mathbf{x}}) + \mathcal{O}(M), \end{cases} \quad \text{where} \quad \begin{cases} \tilde{\rho}_0^{(0)} \in \mathbb{R}^+, \\ \tilde{p}_0^{(0)} \in \mathbb{R}, \\ \nabla_{\tilde{\mathbf{x}}} \cdot \tilde{\mathbf{u}}_0^{(0)} = 0, \end{cases}$$

and the boundary values $\tilde{\rho}_b$, $\tilde{\mathbf{u}}_b$ and $\tilde{p}_b$ satisfy

$$\begin{cases} \tilde{\rho}_b(\tilde{\mathbf{x}},\tilde{t}) = \tilde{\rho}_b^{(0)} + \mathcal{O}(M) \\ \tilde{p}(\tilde{\mathbf{x}},\tilde{t}) = \tilde{p}_b^{(0)} + \mathcal{O}\left(M^2\right), \\ \tilde{\mathbf{u}}(\tilde{\mathbf{x}},\tilde{t}) = \tilde{\mathbf{u}}_b^{(0)}(\tilde{\mathbf{x}}) + \mathcal{O}(M), \end{cases} \quad \text{where} \quad \begin{cases} \tilde{\rho}_b^{(0)} \in \mathbb{R}^+, \\ \tilde{p}_b^{(0)} \in \mathbb{R}, \\ \int_{\partial\Omega} \tilde{\mathbf{u}}_b^{(0)} \cdot \mathbf{n} = 0, \end{cases}$$

the link between the low Mach number solution of Euler system and the long time solution of a linear wave system can also be performed at the continuous and the discrete levels [17]. Then, the results of the present paper can be extended. More precisely, if the numerical flux for the full Euler system conserves contacts (e.g., exact Godunov, Roe, HLLC) and if the mesh is simplicial, the numerical scheme is accurate at low Mach number flows. However, the case of a more general pressure law or where $\tilde{\rho}^{(0)}$ is no more uniform needs more investigation.

Last, we would like to point out that with high order numerical schemes, it is sometimes hard to tell the difference between a scheme that is low Mach number accurate and a scheme that is not low Mach number accurate. Especially, we observed that the difference cannot rely on the eyeball metric on isovalues. A more robust criterion for estimating the low Mach number consists in the assessment of the pressure fluctuations, which should scale as $\mathcal{O}\left(M^2\right)$, and the discrete divergence of the velocity, which should scale as $\mathcal{O}(M)$.

REFERENCES

[1] D. S. Balsara and D. S. Spicer, A staggered mesh algorithm using high order Godunov fluxes to ensure solenoidal magnetic fields in magnetohydrodynamic simulations, Journal of Computational Physics, 149 (1999), pp. 270–292.

[2] W. Barsukow, Truly multi-dimensional all-speed schemes for the Euler equations on Cartesian grids, Journal of Computational Physics, 435 (2021), p. 110216.

[3] F. Bassi, C. De Bartolo, R. Hartmann, and A. Nigro, A discontinuous Galerkin method for inviscid low Mach number flows, J. Comput. Phys., 228 (2009), pp. 3996–4011, https://doi.org/10.1016/j.jcp.2009.02.021.

[4] F. Bassi and S. Rebay, High-order accurate discontinuous finite element solution of the 2d Euler equations, Journal of computational physics, 138 (1997), pp. 251–285, https://doi.org/10.1006/jcph.1997.5454.

[5] W. Boscheri, G. Dimarco, R. Loubère, M. Tavelli, and M.-H. Vignal, A second order all Mach number IMEX finite volume solver for the three dimensional Euler equations, Journal of Computational Physics, 415 (2020), p. 109486, https://doi.org/https://doi.org/10.1016/j.jcp.2020.109486.

[6] W. Boscheri, M. Dumbser, M. Ioriatti, I. Peshkov, and E. Romenski, A structure-preserving staggered semi-implicit finite volume scheme for continuum mechanics, Journal of Computational Physics, 424 (2021), p. 109866, https://doi.org/https://doi.org/10.1016/j.jcp.2020.109866.

[7] F. Bouchut, E. Franck, and L. Navoret, A low cost semi-implicit low-Mach relaxation scheme for the full Euler equations, Journal of Scientific Computing, 83 (2020), pp. 1–47, https://doi.org/https://doi.org/10.1007/s10915-020-01206-z.

[8] F. Brezzi and M. Fortin, Mixed and hybrid finite element methods, vol. 15, Springer Science & Business Media, 2012, https://doi.org/10.1007/978-1-4612-3172-1.

[9] S. Busto, L. Río-Martín, M. E. Vázquez-Cendón, and M. Dumbser, A semi-implicit hybrid finite volume/finite element scheme for all Mach number flows on staggered unstructured meshes, Applied Mathematics and Computation, 402 (2021), p. 126117.

[10] C. Chalons, M. Girardin, and S. Kokh, An all-regime Lagrange-projection like scheme for 2d homogeneous models for two-phase flows on unstructured meshes, Journal of Computational Physics, 335 (2017), pp. 885–904.

[11] F. Cordier, P. Degond, and A. Kumbaro, An asymptotic-preserving all-speed scheme for the Euler and Navier–Stokes equations, Journal of Computational Physics, 231 (2012), pp. 5685–5704.

[12] P. Degond and M. Tang, All speed scheme for the low Mach number limit of the isentropic Euler equations, Communications in Computational Physics, 10 (2011), pp. 1–31.

[13] S. Dellacherie, P. Omnes, and F. Rieper, The influence of cell geometry on the Godunov scheme applied to the linear wave equation, Journal of Computational Physics, 229 (2010), pp. 5315–5338, https://doi.org/10.1016/j.jcp.2010.03.012.

[14] G. Dimarco, R. Loubere, V. Michel-Dansac, and M.-H. Vignal, Second-order implicit-explicit total variation diminishing schemes for the Euler system in the low Mach regime, Journal of Computational Physics, 372 (2018), pp. 178–201, https://doi.org/10.1016/j.jcp.2018.06.022.

[15] G. Dimarco, R. Loubère, and M.-H. Vignal, Study of a new asymptotic preserving scheme for the Euler system in the low Mach number limit, SIAM J. Sci. Comput., 39 (2017), pp. A2099–A2128, https://doi.org/10.1137/16M1069274.

[16] M. Feistauer and V. Kučera, On a robust discontinuous Galerkin technique for the solution of compressible flow, Journal of Computational Physics, 224 (2007), pp. 208–221, https://doi.org/10.1016/j.jcp.2007.01.035.

[17] T. Galié, J. Jung, I. Lannabi, and V. Perrier, Extension of an all-mach roe scheme able to deal with low mach acoustics to full euler system, ESAIM: Proceedings and Surveys, (2023), https://univ-pau.hal.science/hal-04164990.

[18] G. Gallice, A. Chan, R. Loubère, and P.-H. Maire, Entropy stable and positivity preserving Godunov-type schemes for multidimensional hyperbolic systems on unstructured grid, Journal of Computational Physics, 468 (2022), p. 111493, https://doi.org/https://doi.org/10.1016/j.jcp.2022.111493.

[19] S. Gottlieb, C.-W. Shu, and E. Tadmor, Strong stability-preserving high-order time discretization methods, SIAM review, 43 (2001), pp. 89–112, https://doi.org/10.1137/S003614450036757X.

[20] H. Guillard, On the behavior of upwind schemes in the low Mach number limit. IV: P0 approximation on triangular and tetrahedral cells, Computers & Fluids, 38 (2009), pp. 1969–1972, https://doi.org/10.1016/j.compfluid.2009.06.003.

[21] H. Guillard and B. Nkonga, On the behaviour of upwind schemes in the low Mach number limit: A review, Handbook of Numerical Analysis, 18 (2017), pp. 203–231, https://doi.org/10.1016/bs.hna.2016.09.002.

[22] H. Guillard and C. Viozat, On the behaviour of upwind schemes in the low Mach number limit, Computers & fluids, 28 (1999), pp. 63–86, https://doi.org/10.1016/S0045-7930(98)00017-6.

[23] D. Iampietro, F. Daude, P. Galon, and J.-M. Hérard, A Mach-sensitive splitting approach for Euler-like systems, ESAIM: Mathematical Modelling and Numerical Analysis, (2018), https://doi.org/10.1051/m2an/2017063, https://hal.archives-ouvertes.fr/hal-01466827.

[24] J. Jung and V. Perrier, Long time behavior of finite volume discretization of symmetrizable linear hyperbolic systems, IMA Journal of Numerical Analysis, (2021).

[25] J. Jung and V. Perrier, Steady low Mach number flows: identification of the spurious mode and filtering method, Journal of Computational Physics, (2022), p. 111462, https://doi.org/10.1016/j.jcp.2022.111462.

[26] S. Klainerman and A. Majda, Singular limits of quasilinear hyperbolic systems with large parameters and the incompressible limit of compressible fluids, Communications on pure and applied Mathematics, 34 (1981), pp. 481–524.

[27] S. Klainerman and A. Majda, Compressible and incompressible fluids, Communications in Pure Applied Mathematics, 35 (1982), pp. 629–651, https://doi.org/10.1002/cpa.3160350503.

[28] R. Klein, Semi-implicit extension of a godunov-type scheme based on low mach number asymptotics i:

One-dimensional flow, Journal of Computational Physics, 121 (1995), pp. 213–237.
[29] B. Müller, Low Mach number asymptotics of the Navier-Stokes equations and numerical implications, in VKI Lecture Series on Computational fluid dynamics, 1999, pp. 1–52.
[30] S. Noelle, G. Bispen, K. R. Arun, M. Lukáčová-Medviďová, and C.-D. Munz, A weakly asymptotic preserving low Mach number scheme for the Euler equations of gas dynamics, SIAM J. Sci. Comput., 36 (2014), pp. B989–B1024, https://doi.org/10.1137/120895627.
[31] M. Parisot and J.-P. Vila, Centered-potential regularization for the advection upstream splitting method, SIAM J. Numer. Anal., 54 (2016), pp. 3083–3104, https://doi.org/10.1137/15M1021817.
[32] F. Rieper, On the dissipation mechanism of upwind-schemes in the low Mach number regime: A comparison between Roe and HLL, Journal of Computational Physics, 229 (2010), pp. 221–232, https://doi.org/10.1016/j.jcp.2009.09.043.
[33] F. Rieper, A low-Mach number fix for Roe's approximate Riemann solver, Journal of Computational Physics, 230 (2011), pp. 5263–5287, https://doi.org/10.1016/j.jcp.2011.03.025.
[34] F. Rieper and G. Bader, The influence of cell geometry on the accuracy of upwind schemes in the low Mach number regime, Journal of Computational Physics, 228 (2009), pp. 2918–2933, https://doi.org/10.1016/j.jcp.2009.01.002.
[35] S. Schochet, Fast singular limits of hyperbolic PDEs, Journal of differential equations, 114 (1994), pp. 476–512, https://doi.org/10.1006/jdeq.1994.1157.
[36] M. Tavelli and M. Dumbser, A pressure-based semi-implicit space–time discontinuous Galerkin method on staggered unstructured meshes for the solution of the compressible Navier–Stokes equations at all Mach numbers, Journal of Computational Physics, 341 (2017), pp. 341–376.
[37] A. Thomann, G. Puppo, and C. Klingenberg, An all speed second order well-balanced IMEX relaxation scheme for the Euler equations with gravity, Journal of Computational Physics, 420 (2020), p. 109723, https://doi.org/https://doi.org/10.1016/j.jcp.2020.109723.
[38] E. F. Toro, Riemann solvers and numerical methods for fluid dynamics, Springer-Verlag, Berlin, third ed., 2009, https://doi.org/10.1007/b79761. A practical introduction.
[39] G. Volpe, Performance of compressible flow codes at low Mach numbers, AIAA journal, 31 (1993), pp. 49–56, https://doi.org/10.2514/3.11317.
[40] M. Wallraff, T. Leicht, and M. Lange-Hegermann, Numerical flux functions for Reynolds-averaged Navier–Stokes and k–ω turbulence model computations with a line-preconditioned p-multigrid discontinuous Galerkin solver, International Journal for Numerical Methods in Fluids, 71 (2013), pp. 1055–1072, https://doi.org/10.1002/fld.3702.
[41] J. Zeifang, K. Kaiser, A. Beck, J. Schütz, and C.-D. Munz, Efficient high-order discontinuous Galerkin computations of low Mach number flows, Communications in Applied Mathematics and Computational Science, 13 (2018), pp. 243–270, https://doi.org/10.2140/camcos.2018.13.243.